Nature Communications

https://doi.org/10.1038/s41467-026-72488-4

Article in Press

Shock-scattering micro-histotripsy-aided fine needle aspiration for enhanced biomarker profiling and cytopathology

Received: 11 April 2025

Accepted: 14 April 2026

Cite this article as: Wang, J., Kedarisetti, P., McAlister, E.A. *et al.* Shock-scattering micro-histotripsy-aided fine needle aspiration for enhanced biomarker profiling and cytopathology. *Nat Commun* (2026). https://doi.org/10.1038/s41467-026-72488-4

Joy Wang, Pradyumna Kedarisetti, Ewan A. McAlister, Matthew G. Mallay, Jeffrey K. Woodacre, Benjamin A. Adam, Remegio J. Maglantay, Juan Jovel, Frank R. Wuest, Jeremy A. Brown & Roger J. Zemp

Shock-Scattering Micro-Histotripsy-Aided Fine Needle Aspiration for Enhanced Biomarker Profiling and Cytopathology

Joy Wang[1,2*], Pradyumna Kedarisetti[3], Ewan A. McAlister[3], Matthew G. Mallay[4], Jeffrey K. Woodacre[5], Benjamin A. Adam[6], Remegio J. Maglantay[6], Juan Jovel[7], Frank R. Wuest[2], Jeremy A. Brown[8], Roger J. Zemp[1,3*]

[1*]Department of Biomedical Engineering, University of Alberta, Edmonton, T6G 2E1, Alberta, Canada.
[2]Department of Oncology, University of Alberta, Edmonton, T6G 1Z2, Alberta, Canada.
[3]Department of Electrical and Computer Engineering, University of Alberta, Edmonton, T6G 2E1, Alberta, Canada.
[4]SoundBlade Medical Inc., Halifax, B3H 4R2, Nova Scotia, Canada.
[5]Daxsonics Inc., Halifax, B3H 4R2, Nova Scotia, Canada.
[6]Department of Laboratory Medicine and Pathology, University of Alberta, Edmonton, T6G 287, Alberta, Canada.
[7]Faculty of Veterinary Medicine, University of Calgary, Calgary, T2N 4Z6, Alberta, Canada.
[8]Department of Electrical and Computer Engineering, Dalhousie University, Halifax, B3H 4R2, Nova Scotia, Canada.

*Corresponding author(s). E-mail(s): joy3@ualberta.ca; rzemp@ualberta.ca;

Abstract

Core needle biopsy is the gold standard procedure for sampling tissues for pathology-based diagnostics. However, it produces significant tissue damage and may lead to undue pain and risk of complications such as infections. Alternatives such as fine needle aspiration and liquid biopsy have not yet achieved the same widespread utility owing to the limited abundance of cells and relevant biomarkers

in extracted samples. Here we introduce a shock-scattering micro-histotripsy-aided fine needle aspiration technology which uses cavitation to liquefy nano-liter to micro-liter volumes to produce tissue homogenates with both intact and lysed cells. It permits not only conventional cytopathology with high success but sufficient high-quality tissue homogenates to enable reliable ancillary testing such as genetic biomarker profiling and even whole genome sequencing with improved quality compared to formalin-fixed samples. Our approach represents an advance in tissue diagnostics with orders of magnitude less damage than core-needle biopsy procedures.

Keywords: diagnostics, fine-needle aspiration, histotripsy, oncology, whole genome sequencing

1 Introduction

Core needle biopsy (CNB) has become the gold standard for diagnosis of many cancers including in the breast, prostate, liver, lung or lymph nodes, due to high specificity, low false-negative rate, and its ability to sample tissue with intact structural characteristics[1, 2]. Despite the many advantages of core needle biopsies, there still exist barriers to timely cancer diagnosis. Larger caliber needles, such as 9-gauge core biopsy needles, are painful[3] and carry higher risk of negative side effects such as infection[4], bleeding[3], hematoma[5] and needle tract seeding[6]. These complications result in patient anxiety, and resistance to initial or repeat biopsies leading to missed diagnoses or unsuitable treatment. The risks associated with CNB can deter physicians from referring low-risk patients for biopsy. In some institutions, over 30% of patients who underwent breast cancer screening were diagnosed with BI-RADS category 3 lesions and were recommended for only a 6-month follow-up imaging rather than biopsy[7]. This is concerning when some studies have found patient non-compliance with short interval follow-ups to be 29%[8]. There is likely an unknown statistic of patients who did not receive timely diagnosis of their diseases whose prognoses may have been negatively affected due to delays in diagnosis and treatment. CNB is also expensive to perform, being three times as expensive as fine needle aspiration biopsy (FNAB)[9, 10], and requiring additional scheduling of appointments, resulting in a heavier burden on medical systems[11].

Comparatively, FNAB is less invasive than core needle biopsy with much lower incidence of the risks associated with CNB[12, 13]. While FNAB has lower sensitivity than CNB on average (74% vs 87%)[14], it has the benefit of being a same-day procedure, thus lowering burden on the medical system, and helping patients avoid unnecessary psychological distress[15, 16]. FNAB was historically popular, with success in cytopathological analysis of aspirates for cancer diagnosis[17]. However, FNAB is no longer as prevalent in cancer diagnostics in recent decades since the rise of CNB due to multiple disadvantages. A primary barrier to the use of FNAB is the high rate of sampling inadequacy, with one review finding an inadequate sample rate of up to 12.8% for image-guided FNAB[18]. FNAB also requires the presence of a specialized

cytopathologist to assess sample quality. One study compared inadequate sampling rate of 22-gauge FNAB when performed by pathologists or non-pathologist specialists. Inadequate sample rates increased from 7.7% to 24.8% when performed by pathologists or other specialist physicians, respectively[19]. Furthermore, FNAB provides a lower quantity of tissue material for downstream analysis than CNB[20]. As such, there is an unmet need for expanding and improving on the tissue sampling capabilities of FNAB in order to achieve more powerful and accurate diagnostics while maintaining the faster turnaround times and minimally invasive nature of FNAB.

Liquid and blood biopsies have become increasingly popular as a minimally-invasive alternative to conventional core needle biopsies. Liquid biopsy refers to the detection of disease biomarkers from bodily fluids such as blood, cerebrospinal fluid, or urine. Blood biopsy in particular has been explored extensively for use in screening and molecular characterization of cancer due to the challenges associated with traditional biopsies. Invasive biopsies are severely limited in their utility for active surveillance and prognostic profiling throughout treatment for response monitoring due to their invasive nature, high cost and low patient compliance. Additionally, tumors tend to be heterogeneous and constantly evolving, making it difficult to obtain comprehensive tumor profiles with traditional biopsies[21]. With blood biopsies, circulating tumor cells, tumor-derived exosomes, tumor proteins, and circulating tumor-derived nucleic acids like DNA, mRNA, and miRNA can be isolated from patient blood samples and analyzed[22]. However, liquid biopsies may have a narrow diagnostic window as it is difficult to detect biomarkers present at low concentrations at early disease stages.

Microbubble or nanodroplet-enhanced sonication of tumors have recently shown promise for enhancing the detectable biomarker levels present in blood, potentially addressing the current limitations of blood biopsy. D'Souza *et al.* first described a strategy for blood biomarker amplification and localization using ultrasound to overcome challenges faced by blood biopsy techniques[23]. Their work showed that the application of high-intensity, low-frequency ultrasound to tumor cells can significantly increase tumor protein biomarkers available in the blood, and that this effect is specific to the direct application of ultrasound to the tumor. Forbrich *et al.* extended the work on ultrasound-enhanced biomarker release by introducing lipid-stabilized microbubbles which further amplify biomarker release by reducing the cavitation energy required for sonoporation to occur[24, 25]. Paproski *et al.*, subsequently demonstrated the use of phase-change nanodroplets to enhance RNA biomarker release from cells[26]. Forbrich *et al.*, then compared the efficiency of mRNA and miRNA biomarker release with various sonication procedures with or without nanodroplets[25]. Paproski *et al.* next demonstrated that nanodroplet-aided sonication *in vivo* produced not only enhanced free biomarkers but also orders of magnitude enhancements of extracellular vesicles[27]. These vesicles were demonstrated to contain cellular biomarkers and blood sampling post-sonication led to detection of genetic biomarkers and tumor-specific mutations that were otherwise undetectable. A variant of the technique using phase-changing nanodroplets has also been shown to enhance plasma levels of cancer-derived mRNA and miRNA, and extracellular vesicles[26, 27], however it was concluded that these biomarker levels can vary greatly between patients and biomarker levels still remain

too low for reliable blood biopsy, especially in earlier stages of disease. In association with blood biopsies, a method of using high-intensity focused ultrasound to transiently open the blood-brain barrier and release biomarkers into the blood, known as "sono-biopsy", was developed and recently achieved promising first-in-human trials in glioma patients[28].

Fig. 1 Illustrations of current clinical standards of biopsy compared to our method of shock-scattering micro-histotripsy paired fine-needle aspiration biopsy. Portions of figure created in BioRender. Zemp, R. (2026) https://BioRender.com/yi8pn88, https://BioRender.com/mmtr3hq, https://BioRender.com/xhsqz77, https://BioRender.com/mt28456.

We present here a technique pairing shock-scattering micro-histotripsy tissue ablation with fine-needle aspiration biopsy (MH+FNAB) for a fast, minimally invasive method of cancer diagnosis and prognosis (Fig. 1).

Histotripsy is an emerging ultrasound-based tissue ablation technique using extreme ultrasound pressures to induce cavitation damage of tissues. Sufficiently large peak negative pressures cause dissolved air endogenous to liquids and the interstitial fluids of tissues to form microbubble cavitation clouds[29]. As cavitational microbubbles coalesce and collapse, these bubbles mechanically fractionate adjacent cells, destroying them on a subcellular level[29, 30].

Shock-scattering histotripsy relies on nonlinear propagation to generate high peak-positive-pressure shock-wavefronts which are then phase-inverted when scattering off of gas nucleation sites. This produces high peak negative pressures which nucleates further cavitation nuclei and results in a cavitation cloud which achieves purely mechanical damage without appreciable temperature elevation in the tissue. [31, 29]. While boiling histotripsy also produces a mainly non-thermal mechanism for tissue fractionation across the ablation area, a highly spatially confined center region of the focus does achieve instantaneous thermal vaporization [32]. It is uncertain whether this localized, transient rise in temperature would have an effect on the biomarkers released for diagnostic applications.

Histotripsy has principally used massive transducer systems with low (<2 MHz) frequencies for deep-tissue non-invasive surgical applications. Recently, micro-histotripsy has been introduced using higher frequencies (>5 MHz) and compact form-factor transducers and electronics. Shock-scattering micro-histotripsy produces peak-negative pressures >30 MPa, which exceed the cavitation threshold intrinsic to tissues (-14 to -28 MPa) for single-cycle ultrasound pulses. At a frequency of 6.3 MHz, the formation of sub-millimeter sized cavitation clouds can be achieved[31, 33]. Shock-scattering micro-histotripsy specializes in highly precise cavitation and minimal overall tissue damage that allows for navigating around potentially sensitive structures[34]. For this reason, shock-scattering histotripsy provides a further advantage over boiling histotripsy for minimally invasive diagnostic applications, as boiling histotripsy produces characteristic axially-elongated tadpole-shaped ablation zones [32]. Even at

the highest end of transducer frequencies, boiling histotripsy ablation zones cannot currently be miniaturized as effectively as intrinsic and shock-scattering histotripsy.

Due to the ability for histotripsy to liquefy and disincorporate soft tissues in a precise and non-invasive manner, it is a promising candidate for cancer therapy. Compared to current standard cancer therapy options such as radiation, surgical resection, or thermal ablation, histotripsy offers non-surgical, non-ionizing, and non-thermal bulk removal of tumor mass through mechanical ultrasound cavitation damage[31]. A number of preclinical studies investigating the efficacy of histotripsy for tumor treatment have been performed in recent years, including in hepatocellular carcinoma[35, 36], prostate cancer[37], melanoma[38], cholangiocarcinoma[39], renal cell carcinoma[40], pancreatic cancer[41], osteosarcoma[42], and glioma[43]. Results of preclinical animal trials for liver tumors have been particularly impressive, with tumors treated with complete or partial histotripsy ablation undergoing complete reabsorption of liquefied tumor tissue and complete local tumor regression in over 80% of cases, leaving only a small amount of non-tumoral fibrous scar tissue after 3 months[44, 35].

Despite the extensive and in-depth work on the therapeutic application of histotripsy, there are still very few studies that explore its potential as a minimally invasive diagnostic tool. To date, the only study published for histotripsy-assisted diagnosis of diseases is related to boiling histotripsy-facilitated liquid biopsy. In 2017, Chevillet *et al.*[45] performed a study using three methods of pulsed focused ultrasound to induce release of tumor-derived miRNAs into the blood circulation, of which one ultrasound method was boiling histotripsy for liquefaction of the tumor. They found that boiling histotripsy produced up to a 32-fold increase in plasma quantities of candidate biomarkers within 15 minutes after start of treatment, and levels remained elevated for up to 3 hours. However, since this study, no other work has been published on the subject, perhaps due to the arduous nature of consistent biomarker detection in blood samples. Additionally, no one has explored the potential of shock-scattering histotripsy, which can achieve smaller ablation zones, for similar applications in enhancing biomarkers for disease diagnosis.

The Chevillet *et al.*[45] study intended to maximize biomarker release into the blood by conducting boiling histotripsy treatment in a grid which covered most of the tumor, and mentions that boiling histotripsy liquefaction of tissues is potentially too destructive to justify its use as a replacement for needle biopsies. Their less destructive permeabilization method also released similar amounts of miRNA. Furthermore, they discuss one of their limitations being that they only examined miRNAs as biomarkers due to their increased stability and count in plasma, but have yet to test their method with other biomarker types.

In contrast, our method relies on completely mechanical shock-scattering microhistotripsy, and has a focus on minimizing disturbance to the overall tumor structure. Our method, affecting only 500 nano-liters of volume, addsnegligible damage to a FNA procedure, and aims to provide the most minimally invasive alternative to needle biopsies, while being capable of extracting and detecting many biomarker

types. Our method produces tissue homogenates with both intact and lysed cells, and is proposed for use in shallow tumors, as the high frequency, compact design of the micro-histotripsy transducer (Fig. 2A,B) currently allows for limited treatment depth. It permits not only conventional cytopathology with high success but also sufficient high-quality tissue homogenates to enable reliable ancillary testing such as genetic biomarker profiling and even whole genome sequencing with improved quality compared to formalin-fixed samples. Our approach represents an advance in tissue diagnostics with orders of magnitude less damage than core-needle biopsy procedures.

Cavitational histotripsy has proven its worth as a non-invasive method for precise liquefaction of tissues with minimal risk of off-target effects, and we believe that there is an opportunity for it to fill a niche within the realm of fast, minimally invasive techniques for diagnosis and molecular characterization of cancer.

2 Results

2.1 Preliminary testing: In-vitro histotripsy of cancer cell line pellets

To first demonstrate the utility of shock-scattering micro-histotripsy for massive biomarker release, we performed *in-vitro* experiments using cell pellets.

A pilot experiment was conducted which used our custom 10mm single element piezoelectric shock-scattering micro-histotripsy transducer to cavitate and release biomarkers from centrifuged breast cancer cell pellets. Human breast cancer cells of triple negative subtype with hypermethylation of the BRCA1 gene (HCC-38) were used as an ablation target in these *in-vitro* histotripsy treatments. BRCA1 hypermethylation was chosen as a representative cancer-specific biomarker due to the presence of this epimutation in a large fraction of both hereditary [46] and sporadic [47] breast cancers, as well as ovarian and prostate cancers[46, 48]. Micro-histotripsy was applied to cell pellets to establish varying baseline parameters with respect to voltage, treatment duration, and single- or multi-target treatment. A minimum voltage threshold for cavitation to occur with our histotripsy transducer was first established by cavitating in water, followed by the cell pellet. Running the histotripsy driver board with a supply voltage of -120 VDC was enough to cause sporadic cavitation, but consistent cavitation was only achieved at -160 VDC. Single-target histotripsy was then applied for varying durations up to 2 minutes to cell pellets, acquiring pre- and post-histotripsy supernatant samples for each treatment duration group. Biomarker release tended to increase with increased treatment duration. Multi-target histotripsy was also tested, in which a 2-by-2 grid of spots (4 total) were ablated on the cell pellet for varying time durations before collecting a post-histotripsy sample. The maximum level of biomarker detection was achieved overall by applying histotripsy to 4 focal zones on the pellet for 30 seconds each (Supplementary Data 1), which was the maximum chosen time for the multi-target histotripsy test group in this experiment. The hypermethylated allele of BRCA1 was detected at 97,077-fold higher in concentration in the post-histotripsy sample compared to the pre-histotripsy control. Based on standard dilution curves run

alongside the samples, this equates to about 1 million copies of the hypermethylated BRCA1 allele present in the post-histotripsy sample at the time of sample acquisition. While the total time of histotripsy treatment for the 30sec/multi-target group is equivalent to the 2min/single-target group, the methylated BRCA1 released from the multi-target treatment was over 78 times the amount released in the single-target treatment.

Fig. 2 Micro-histotripsy system and transducer specifications and imaging setup. **(A)** Micro-histotripsy custom driver board connects to a -350 VDC power supply and is driven by a function generator set to cycle at 6.3 MHz with 10 cycles per transmit pulse at a pulse repetition frequency of 1-kHz. The transducer produces an estimated peak-negative pressure of 40 MPa in water, and around 30 MPa *in-vivo* due to attenuation. **(B)** Custom 1-3 piezoelectric composite micro-histotripsy transducer is 10 mm in diameter, small enough to be an easy add-on to the end of a fine needle. **(C)** Schematic of the positioning of imaging and histotripsy transducers, held together by a custom 3D-printed holder, relative to a target tumor. **(D)** Photograph of the custom 3D-printed transducer holder. **(E)** Illustration of experimental method *in vivo* in a mouse model. Portions of figure created in BioRender. Zemp, R. (2026) https://BioRender.com/z3tcz3x, https://BioRender.com/c70v140.

2.2 Cancer-specific DNA and mRNA biomarkers release poorly into the blood circulation

Since blood biopsies have shown promise as a minimally invasive alternative to conventional core needle biopsies, and because our group has previously done work enhancing cancer-released vesicles in chicken embryos using nanodroplet-enhanced FUS[27], the initial focus of this study was to use shock-scattering micro-histotripsy for enhancement of blood biopsy. We applied micro-histotripsy in flank tumor-bearing mice using our custom shock-scattering micro-histotripsy transducer. The custom transducer is only 10mm in diameter with a 7-mm focal length that produces a sub-millimeter ablation zone. We anticipated that micro-histotripsy liquefaction of sub-millimeter volumes of tumor tissue could release massive amounts of biomarkers into the blood which could be sampled via tail vein. However, what we found after months of *in vivo* experiments in over 20 mice was that the DNA and mRNA biomarkers we were searching for were being inhibited by physiological barriers, affecting entry and spread into the bloodstream, and we could rarely produce detectable plasma concentrations of our biomarkers (Supplementary Figure 1). In one attempt, blood samples were taken from a mouse immediately after histotripsy, at 20 minutes, and at 1, 2, 3, 4, and 5 days after histotripsy but found no qPCR amplification of the target biomarkers. These results could be explained by the destructive nature of histotripsy cavitation, which may destroy micro-vasculature around the ablation area while causing clotting factors to activate, preventing larger biomarkers like DNA and mRNA from entering circulation. It is of note that smaller nucleic acids, like miRNAs have been shown to have better release than larger mRNAs in previous blood biopsy studies[25], and may be better biomarker candidates for histotripsy-enhanced biomarker release into blood. However, we chose instead to explore the potential for direct local sampling of liquefied tissue through FNA.

2.3 Qualitative effects of micro-histotripsy

For shock-scattering micro-histotripsy paired FNA (MH+FNAB) to be a suitable preliminary diagnostic test, its effects should be small enough to have negligible impact on further core needle biopsies while producing massive biomarker release for optimal molecular profiling of the tumor. In order to determine the qualitative effects of our custom micro-histotripsy system on the tumor and surrounding tissue, *in vivo* xenograft tumors in mice were tracked during micro-histotripsy treatment by real-time ultrasound and photoacoustic (PA) imaging, and evaluated post-procedure by histological analysis of the excised tumor. Under real time ultrasound imaging, micro-histotripsy in subcutaneous xenograft tumors was shown to produce ablation zones of less than 1 mm in width and between 1-2 mm in length by the end of a 3 minute treatment procedure (Supplementary Movie 1). However, due to the hyperechoic nature of the cavitation bubble under ultrasound, this measurement is larger than the true scale of the ablation zone which is closer to 0.5 mm in width and 1 mm in length when examined microscopically post-excision (Fig. 3D). Using the ultrasound B-scans, mean ablation volume was also estimated to be 0.124 mm^3 (+/- 0.028 mm^3, std. error) across 5 different cavitation events. This damage to the tumor is around 1% of tumor

volume even after accounting for damage from fine-needle insertion. The histotripsy ablation is initially observed to affect a spherical zone of about 0.5 mm in diameter at the start of treatment. As the affected tissue is liquefied, the ablation zone gradually lengthens in the axial direction to the transducer during the course of the 3 minute treatment up to around 1 mm. Aspiration using a 25-gauge fine-needle paired with micro-histotripsy produces a much smaller volume of tissue damage of about 1.8% of the damage volume produced by one pass of a 9-gauge core needle assuming a 3 cm biopsy depth (assume cylinder with 0.5 mm diameter vs 3.76 mm diameter).

Fig. 3 Qualitative effects of shock-scattering micro-histotripsy cavitation on tumor tissue. **(A)** Ultrasound images showing mouse tumor during histotripsy, post-histotripsy liquid cavity, and FNA of liquid in histotripsy cavity. The dotted blue line indicates tumor boundary, and the dotted yellow line indicates the 25-gauge fine needle. **(B)** Oxygen-saturation PA imaging overlay on B-mode ultrasound of *in vivo* mouse tumor before and immediately post-histotripsy. Histotripsy ablation cavity is indicated by a yellow circle, and PA SNR for the area within the tumor boundary is shown for each respective image. **(C)** Excised mouse flank tumor following histotripsy treatment and euthanasia of the mouse. The tumor is sitting atop a No.21 surgical scalpel blade, and the tiny "hole" (blue arrow) from the histotripsy cavitation is visible on the face of the tumor. **(D)** H&E sections of adjacent (left) and on-target (right) slices of the same region of the same tumor treated by micro-histotripsy cavitation. Histotripsy produces a sharp boundary at the edge of the treatment zone without disturbing or affecting the morphology of the remaining tumor tissue in the surroundings. Yellow circle indicates region of histotripsy ablation. Red arrows show loosened cells and tissue likely to be aspirated into the sample.

Micro-histotripsy produces a very sharp boundary between dead and live cells at the edge of the histotripsy focal zone (Fig. 3D) with no discernible damage to tissue outside of the focal zone. Apart from the approximately 1mm^3 histotripsy focal zone, the remainder of the tumor remains structurally and morphologically intact following micro-histotripsy treatment, suggesting that further acquisition of core biopsies, if deemed necessary, should not be impacted. Micro-histotripsy produced nearly complete liquefaction of the target area into subcellular debris, with some intact nuclei and cells observable within the lysate. Some pooling of blood alongside the liquefied tissue can be seen in the histotripsy cavity via PA imaging immediately post-treatment (Fig. 3B). PA images of the tumor show a larger signal concentrated around the ablation zone with greater signal-to-noise ratio (SNR) immediately post-histotripsy compared to pre-histotripsy (33.30 vs 21.54, respectively). Using this visualization method, PA imaging can allow for further guidance of fine-needle aspiration if tumor heterogeneity makes ultrasound needle guidance difficult.

Our shock-scattering micro-histotripsy technique produced no observable heat damage to targeted tissues or surrounding tissue, as shown by the lack of whitish discoloration seen in test tissues exposed to micro-histotripsy treatment for extended periods of time up to 15 minutes (Supplementary Figure 2A). Additionally, by using PA guidance in pre-histotripsy alignment to avoid highly vascularized areas, we are able to minimize hemorrhage and edema around the treatment area and the area of the tumor as a whole (Supplementary Figure 2B). However, during certain trials in which histotripsy treatment was applied too shallowly on the mice, the micro-histotripsy did break skin and cause edema and purple-ish bruising on the flanks of the mice which healed within 5 days. The occurrence of such scenarios was based on the proficiency of the investigators applying the treatment, and was consistently avoided in later trials as the investigators became more comfortable with the procedure. No discomfort was observed in the mice when histotripsy was applied on-target, and further experiments applied histotripsy at least 2 mm in depth from the surface of the skin. Following histotripsy treatments and recovery from anesthesia, mice were immediately alert and mobile, and displayed no signs of pain, morbidity, or other abnormal behaviors in the following days. This allowed for up to three sets of histotripsy treatments per mouse, each one week apart. Based on good health conditions of the mice up to the end of the third and final treatment, there may be possibility for more treatments over a longer period, or with greater frequency. Due to initial ethical guidelines set for total blood volume allowed to be drawn per mouse during the planning stages of these experiments, longer term or higher frequency treatment regimens have yet to be tested.

2.4 Enhanced detection of cancer-specific BRCA1 DNA methylation

One envisioned way of assessing the malignancy of a suspicious lesion is to sample cancer-specific markers from a fine-needle aspiration procedure. We sought to do this with our histotripsy aided fine-needle aspiration procedure using a xenograft mouse model of breast cancer (Fig. 2). Micro-histotripsy paired with fine-needle aspiration (MH+FNAB) significantly increased detection of epigenetic biomarkers compared to

pre-histotripsy controls and conventional FNAB (Fig. 4A). Hypermethylation of CpG islands in the BRCA1 promoter region is known to be a strong indicator of hereditary breast cancer risk and is present in sporadic breast tumors compared to patients with benign tumors[47], and was therefore chosen as a representative epimutation for testing. This alone may not conclude the presence of cancer, but could be one of multiple markers in a panel that could inform on cancer presence. As proof of principle, here we focus on hypermethylation of BRCA1 promoter which is one of many epimutations that are utilized for cancer diagnosis. The presence of the hypermethylated allele of the BRCA1 promoter had a median fold-increase of 3174.9 (delta-CT 95% CI: 8.28 - 14.69; 311.37 - 26432 on normal scale) in the MH+FNAB samples relative to the pre-histotripsy group (P = 4.58e-5), while the non-methylated allele amplified by a median of 238-fold (P = 0.0035, delta-CT 95% CI: 5.35 - 8.74; 40.64 - 427.9 on normal scale) in the MH+FNAB sample compared to pre-histotripsy. This indicates lower proportion of the non-methylated allele and confirms hypermethylation of the BRCA1 promoter, but also signifies overall improved BRCA1 biomarker detection in the MH+FNAB treated group. In the pathologist-performed conventional FNA group, detectable levels were not achieved for either of the BRCA1 alleles in these samples. As an indicator for change in total DNA material extracted by pairing MH with FNAB, we evaluated beta-actin quantities detected between samples from the pre- and post-histotripsy treatment groups, and saw a significant (P = 0.0027) median increase of 1,374-fold (delta-CT 95% CI: 6.68 - 12.97; 102.36 - 8017 on normal scale) in the MH+FNAB group relative to the conventional FNAB group. This would suggest that to some extent, the enhanced biomarker quantities available for detection in the MH+FNAB group is due to an overall increase in the genetic material made available for FNAB following MH, which liquefies tougher solid tissue into fluid easily aspirated by needle.

Fig. 4 Micro-histotripsy liquefaction of tumors enhances cancer-specific BRCA1 epimutation release. **(A)** Unmethylated and methylated alleles of BRCA1 promoter region were detected via qPCR in conventional FNA, pre-histotripsy FNA, or histotripsy+FNA samples (n=3 tumors conventional FNA, n=15 tumors pre-histotripsy, n=9 tumors MH+FNA). DNA copies detected are plotted on a log10 scale, error bars represent standard error. Both unmethylated and methylated alleles of the BRCA1 promoter region were significantly higher in the histotripsy+FNA group compared to the conventional FNA (p = 0.00084 and 0.00015, respectively) and pre-histotripsy FNA (p = 0.0035 and 4.58e-5, respectively) controls. There is no significant difference in BRCA1 biomarker detection between conventional and pre-histotripsy FNA samples (p = 0.43 for unmethylated allele and p = 0.065 for methylated allele). **(B)** Representative qPCR curves for pre-histotripsy FNA control and post-histotripsy FNA samples. Groups were compared using two-sided Wilcoxon signed rank exact test (paired comparisons) and two-sided Wilcoxon rank sum test (unpaired comparisons) with Bonferroni correction for multiple comparisons. Mean and standard error are indicated.*P < 0.05; **P < 0.01; ***P < 0.001; ns P > 0.05.

2.5 Enhanced Detection of Histotripsy-Amplified mRNA Biomarkers for Cancer Subtyping

In breast cancer diagnosis, analysis of hormone receptor status of the tumor is a standard-of-care test that informs the clinician of cancer prognosis and suitable treatment strategies. Normally, core biopsies would need to be taken and multi-day immunohistochemical analysis would have to be performed on the samples to determine hormone receptor status. Our technique is capable of detecting mRNA biomarkers for indicating hormone receptor status with a much faster turnaround time than standard immunostaining. MH+FNAB treatment significantly enhanced the detectable levels of the relevant hormone receptor mRNA levels corresponding to breast cancer subtype (Fig. 5A). With xenograft tumors originating from a human ER/PR+ breast cancer cell line (MCF7), significantly higher quantities of ER($P = 0.048$) and PR($P = 0.036$) mRNA were detected via RT-qPCR in the MH+FNAB treatment group relative to the pre-histotripsy FNAB control. Median 2645-fold (delta-CT 95% CI: 2.14 - 23.0; 4.41 - 8.38e6 on normal scale) and 5599-fold (delta-CT 95% CI: 5.02 - 22.29; 32.44 - 5.12e6 on normal scale) increases were detected for ER and PR, respectively. Conversely, in experiments using xenograft tumors originating from a human triple-negative breast cancer cell line (HCC-38), no significant difference was found in the mRNA expression of either ER or PR ($P > 0.05$). These results are reflective of the hormone receptor status seen in direct lysis controls from their respective cell lines, and correctly indicate ER/PR over-expression in a luminal breast cancer subtype or lack thereof in a triple-negative subtype.

Fig. 5 Micro-histotripsy liquefaction of tumors enhances cancer subtype-specific hormone receptor mRNA biomarker release. **(A)** ER, PR, and HER2 mRNA levels were quantified in conventional FNA, pre-histotripsy FNA, or histotripsy+FNA samples in a luminal breast cancer (ER/PR+) or TNBC cancer type (luminal n=8 pre-histotripsy, n=6 post-histotripsy; TNBC n=18 pre-histotripsy, n=11 post-histotripsy; samples in duplicate). mRNA copies detected are plotted on a log10 scale, error bars represent standard error. ER and PR mRNA levels were significantly higher post-histotripsy versus control ($p = 0.048$ and 0.036, respectively) in the luminal subtype, while no difference was observed in the TNBC subtype ($p = 0.55$ and 0.61, respectively). HER2 mRNA levels were amplified post-histotripsy in the TNBC subtype ($p = 2.57e\text{-}4$) despite both cell types used being known HER2 negative subtypes. **(B)** Representative gene expression qPCR curves for pre-histotripsy FNA control and post-histotripsy FNA samples. **(C)** Control experiment against a true HER2+ cell line shows that the HER2- cancer types still amplify under qPCR due to primer sensitivity, but significantly less quantity of HER2 mRNA is detected compared to HER2+ control ($p = 0.0095$) (n=2 different cell lines each for HER2+ and HER2- groups, in triplicate). Groups were compared using two-sided Wilcoxon signed rank exact test (paired comparisons) and two-sided Wilcoxon rank sum test (unpaired comparisons) with Bonferroni correction for multiple comparisons. *$P < 0.05$; **$P < 0.01$; ***$P < 0.001$; ns $P > 0.05$.

Contrary to our initial assumptions, despite both MCF7 and HCC-38 cells being HER2 negative, the qPCR primers we used were able to detect increased levels of HER2 mRNA in the TNBC tumor type (P = 2.57e-4) in the MH+FNAB group compared to the pre-histotripsy FNAB counterpart. However, as this result was observed even in the cell line lysis controls, it is most likely an effect of the qPCR primer's high sensitivity to baseline levels of HER2 expression. To confirm this, control tests were performed alongside proper HER2-positive cell lines (Fig. 5C), and despite the HER2-negative cell lines producing qPCR amplification, these samples still had significantly less (P = 0.0095) HER2 expression than HER2-positive controls. In the case of HER2 expression, it may be necessary for future studies to determine a more suitable qPCR primer for differentiating between known HER2-positive and HER2-negative cells.

2.6 Micro-Histotripsy Paired Fine-Needle Aspiration Enhances Cell and Tissue Sampling for Cytopathology

To test whether the applications for shock-scattering micro-histotripsy paired FNA could extend beyond molecular analyses, we asked cytopathologists to examine the adequacy of histotripsy lysate samples for use in histology. Following our procedures for *in vivo* micro-histotripsy biomarker release from flank tumors in mice, but using the B16F10 mouse melanoma cell line, FNAB and MH+FNAB samples were prepared as cell smears and cell pellets for cytopathological analysis. The total sample, which was made up of tissue aspirate drawn into 100 µL of EDTA buffer pre-loaded into the needle head, had a 20 µL fraction for smearing while the remainder was centrifuged for a cell pellet, keeping the supernatant for qPCR analysis. Consistent extraction of cellular material was achieved in FNAB+MH samples, while conventional FNAB samples were relatively unreliable during our attempts to extract material for analysis. Only 1 of 5 attempts at conventional FNAB was able to produce sufficient material for microscopic imaging.

Fig. 6 Cell smears and sectioned cell pellet slides for cytology analysis. **(A)** Cell smears and FFPE sectioned cell pellet slide comparisons between conventional FNAB, pre-histotripsy FNA, and MH+FNAB, stained with H&E and anti-S100A4 immunohistochemistry. In the pre-histotripsy samples, minimal material for staining and imaging could be extracted even after 5 separate attempts on different mice. In the MH+FNAB samples, mostly loose cells can be seen with some cell clusters (CL), on a backdrop of acellular debris (cloudy pink material in H&E). Cells in the sample exhibit classic signs of malignancy like condensed chromatin and prominent nucleoli (red arrow) as well as melanin expression (*). Cells stain positive for S100A4 (yellow arrows), a standard protein biomarker in melanoma.**(B)** Pathologist-evaluated cell counts per 40X FOV, with pooled scores of 10 FOVs per slide, per pathologist. Two pathologists performed blinded slide reviews on n=12 FNA smears, n=2 histotripsy smears, n=6 FNA pellets, and n=1 histotripsy pellet slides.

Histological analysis of both the cell smears and cell pellets from FNAB+MH samples show high cellularity with predominantly loose single cells, some cell-free nuclei, and some cell clusters. Clear visualization of enlarged nuclei with prominent nucleoli and coarse chromatin confirm malignancy of the cells in the cell pellet images (Fig. 6), and while the cell smear images have poorer visualization, the disorganization and enlargement of nuclei are sufficient to indicate malignancy. Melanin pigment among the cells can also be observed in the H&E images, and the samples stain positive for S100A4 protein, a standard immunohistochemical marker of melanoma, reinforcing the melanoma origin of the samples.

2.7 Whole Genome Sequencing

We further explored the option for auxiliary analyses by performing whole-genome sequencing with our shock-scattering micro-histotripsy paired fine-needle aspiration technique. The supernatant of a centrifuged histotripsy-paired aspiration sample can be used for whole genome sequencing in tandem with cytological analysis of the sample pellet. With core needle biopsies, the standard procedure following extraction of the cores is fixation of the sample in a neutral-buffered formalin solution. This allows for long term preservation of the tissues, as well as enabling the processing of the sample into paraffin-embedded blocks for histological analysis. However, while formalin-fixed core biopsy samples are commonly used for sequencing analysis due to the abundance of sample availability[49], artifacts caused by formalin fixation such as DNA fragmentation and artificial sequence alteration frequently cause issues for sequencing and may disproportionately affect detection of low frequency mutation variants[50]. Using micro-histotripsy paired FNA, we acquired sufficient, fresh, genetic material for whole-genome sequencing from only the supernatant fraction post-centrifugation of the aspirate sample, allowing for sequencing analysis alongside cytopathological analysis on the sample pellet.

DNA quality assessment using DNA gel electrophoresis showed almost no DNA detectable from a 25mg sample of formalin-fixed melanoma tumor (Supplementary Figure 3) after 6 different attempts with various optimizations, most likely due to formalin-catalyzed cross-links causing loss during extraction, as well as extensive degradation of DNA due to fragmentation. The same extraction process with a fresh, non-frozen, non-formalin-fixed tumor (hereby referred to as "fresh tumor") processed with Trizol reagent for DNA extraction yielded more than sufficient DNA for downstream analytics. Fresh tumor DNA was used in all subsequent sequencing steps. DNA extraction from 20 µL of micro-histotripsy aspirate produced sufficient quality and quantity of DNA for sequencing, although some DNA fragmentation was observed (Supplementary Figure 3). However, minor DNA fragmentation may not be an issue for whole genome sequencing, as DNA fragmentation is a commonly applied step in the DNA library preparation process. Around 120 ng of DNA was extracted from the micro-histotripsy aspirate sample without the need for extra pre-amplification prior to library preparation.

We were able to call many mutations in both fresh tumor and histotripsy samples (Supplementary Data 2 and 3), which were distributed following a similar spatial pattern, along all chromosomes (Fig. 7A). Mutations were observed with slightly higher frequency in the histotripsy sample than in the fresh tumor one. As expected from the genome organization, most variants were comprised inside intergenic and intronic regions. Other less prominent categories include non-coding RNA sequences, 3'-UTR and exonic variants (Fig. 7B). We focused on exonic variants and specifically on those that are non-synonymous, i.e. leading to missense proteins (variants that lead to the addition of a different amino acids) or to truncated proteins (giving rise to a stop codon). Respectively, 6,628 and 9,265 non-synonymous exonic variants were detected in the tumor and histotripsy samples, which were located in 2,498 and 3,358 genes. Thus, the number of mutations detected in the histotripsy sample was higher than in the fresh tumor sample. All categories of mutations were detected in greater abundance in the histotripsy sample. Of interest, when the number of mutations in the tumor sample was set as reference (normalized to a value of 1) the abundance of mutations in the histotripsy sample exhibited a 1.2- to >3.5-fold increase in mutation abundance (Fig. 7C). While it is unexpected that the histotripsy sample would exhibit a higher frequency of mutations than a sample from the source tumor, this is most likely due to the histotripsy sample being from concentrated, internal regions of the tumor. In comparison, the tumor sample, which was made by whole-tumor lysis then processing of a portion of the lysate, inevitably contains surrounding non-cancerous or fibrous tissue, diluting the proportion of mutations that can be found within a same-volume sample.

We then screened cancer mutations census included in the Catalogue Of Somatic Mutations In Cancer (COSMIC database)[51] in search of genes that are involved in human cancers and were detected in our libraries. Respectively, 69 and 81 genes that are involved in human cancer, according to COSMIC, were found harboring non-synonymous mutations in our tumor and histotripsy libraries, with some of those having direct associations to melanoma (Supplementary Data 4 and 5).

Finally, since the cells used to induce tumors in our mice harbor the prototypical melanoma mutation BRAF V600E in the mitogen-activated protein kinase (*MAPK*) gene [52], we sought for such mutation in our datasets. That specific mutation was not found in our libraries, nor was any other mutation in the exonic regions of such gene. However, 2 and 44 mutations in the introns of *Braf* were detected in the tumor and histotripsy libraries, respectively.

While coverage estimated from alignments of our libraries to the mouse genome (mm10) showed an average coverage of 3.7X, several methodological considerations support the reliability of our variant calling despite this limitation. First, our samples were obtained through micro-histotripsy-aided fine needle aspiration, which, on the scale of DNA needed for whole-genome sequencing, yields quantities of DNA on the lower end of input requirements. Around 120 ng of DNA was collected in the histotripsy sample, and a pre-amplification step was not used prior to library prep. Second, we employed stringent filtering criteria (minimal sampling depth of 10X and

quality score of 20) that prioritize high-confidence variants over sensitivity, ensuring that detected variants represent genuine mutations rather than artifacts. Key quality control metrics can be found in Supplementary Fig. 4. Third, the successful detection of multiple intronic *Braf* mutations (2 and 44 in tumor and histotripsy libraries, respectively) demonstrates that our sequencing pipeline effectively captured variants in this genomic region when present at detectable levels. The absence of the V600E mutation may reflect: (1) sampling heterogeneity inherent to fine needle aspiration procedures, (2) potential loss of the original driver mutation in subpopulations of tumor cells, or (3) the technical challenges associated with detecting specific variants from limited cellular material. While deeper sequencing would enhance sensitivity, our conservative approach was designed to minimize false positives in the context of samples with inherently limited DNA input, where library preparation artifacts can be more prevalent.

Fig. 7 Mouse melanoma tumor and matching histotripsy sample mutations along the chromosome. **(A)**(top) Mutations found within the genome of a YUMM1.G1 mouse melanoma flank tumor inoculated in a mouse model and (bottom) within the genome of a histotripsy lysate sample extracted via FNA from the same YUMM1.G1 tumor. **(B)** Tumor versus histotripsy lysate DNA mutations per million reads on a log10 scale. **(C)** Number of histotripsy lysate DNA mutations normalized to mutation count in the tumor genome.

3 Discussion

In our study we were able to use shock-scattering micro-histotripsy ablation of tumor tissues to vastly multiply the quantity of cancer biomarkers available to be sampled via fine-needle aspiration biopsy and detected via qPCR, while only producing damage zones within 500 nano-liters of volume.

Although one study has previously looked at the use of histotripsy for detecting biomarkers via blood biopsy[45], their study intended to maximize biomarker release into the blood by conducting boiling histotripsy treatment in a grid which covered most of the tumor. Additionally, they only examined miRNAs as biomarkers due to their increased stability and count in plasma, but still reported only up to 32-fold increase in biomarker detection. In contrast, our method relies on completely mechanical shock-scattering micro-histotripsy, while achieving over 3000-fold enhancement of DNA methylation biomarkers and up to around 5500-fold enhancement of mRNA biomarkers compared to pre-histotripsy controls. Shock-scattering micro-histotripsy affects only 500 nano-liters of tissue volume, adding nearly negligible damage to a FNA procedure, and this technique aims to provide the most minimally invasive alternative to needle biopsies, while being capable of extracting and detecting many biomarker types.

Shock-scattering micro-histotripsy ablation of tumor tissues was shown to be able to amplify detection of our representative epimutational breast cancer biomarker, BRCA1 promoter hypermethylation, over 3000-fold more than our conventional FNA control. Additionally, it was shown that micro-histotripsy aided release of mRNA biomarkers could correctly indicate hormone receptor status for breast cancer subtyping. ER and PR mRNA levels were amplified by over 2 600-fold and 5500-fold, respectively, in an ER/PR+ breast cancer subtype while producing no significant amplification in a triple negative breast cancer subtype. While HER2 was seen being amplified via qPCR in a HER2-negative strain of breast cancer, we were able to show this was a result of PCR primer sensitivity, as a HER2-positive control showed significantly higher amplification.

Furthermore, our study shows that micro-histotripsy paired FNA applications can extend beyond PCR-based genomic analysis to cytopathology and whole-genome sequencing. Micro-histotripsy liquefaction of tumor tissue facilitated FNA sampling and achieved consistent extraction of cellular material adequate for cytopathology, even as our FNA procedures were performed by an untrained non-specialist. The most commonly cited complaints against conventional FNA in the literature are high rate of sampling inadequacy[1, 2], and the need for an on-site experienced cytopathologist[20, 53]. We have shown that our technique using micro-histotripsy overcomes these limitations, and could allow for revitalization of FNA in circumstances where currently, CNB is considered more appropriate.

Micro-histotripsy paired FNA is also capable of extracting sufficient DNA of adequate quality for whole-genome sequencing without the need for pre-amplification

steps, and yielded relevant cancer-specific genomic mutations which matched and exceeded those detected in the excised tumor. Around 120 ng of DNA was extracted from our 20 µL micro-histotripsy aspirate sample without the need for extra pre-amplification prior to library preparation. For context, 1 ng of DNA is theoretically enough for whole-genome sequencing, however, library preparation kits typically recommend at least 100 ng of input DNA for sequencing of larger genomes (Illumina DNA prep kit, 20060060). Single-cell sequencing technologies exist; however, they require pre-amplification steps to produce large copies of the genome, amplifying picograms of DNA into hundreds of nanograms. This process commonly causes certain fragments of the genome to clone better than others, thereby skewing the representation of some genes.

Our work demonstrates the feasibility for micro-histotripsy paired FNA to be incorporated into cancer diagnosis procedures in cases where it is uncertain if a more invasive biopsy is required, and confers several advantages: (1) Micro-histotripsy paired FNA maintains the primary advantages of traditional FNA such as being quick to perform (under 10 minutes for liquefaction plus sampling) and inexpensive, with nearly no increase in tissue damage. (2) Histotripsy samples provide options for simultaneous molecular and cytological characterization of the tumor. (3) Due to the small area of effect of micro-histotripsy, being around 500 nano-liters in volume, this technique leaves ample tumor material even in the case of smaller-sized tumors, and thus does not affect or remove the option for core needle biopsy afterwards if deemed necessary. (4) Micro-histotripsy liquefaction of tumor tissue simplifies sample extraction to the point where it could be consistently performed by individuals untrained in conventional FNA procedures, and therefore negates the limitations of FNAB requiring on-site cytopathologist presence for adequate sampling. (5) The micro-histotripsy paired FNA procedure can be integrated into widely-available clinical ultrasound imaging platforms for imaging guidance, thereby reducing technological barriers to clinical translation.

Although the focus of our study was to provide proof-of-concept for cancer diagnosis and prognosis, micro-histotripsy paired fine-needle aspiration could very similarly be used to assist in evaluation of therapeutic response through tracking of molecular changes within the tumor. With the massive enhancement of biomarker quantities released by shock-scattering micro-histotripsy, it may be easier to track molecular changes in tumors sooner after the start of treatment, reducing the time taken to confirm efficacy of certain treatments and allowing for faster turnaround in case alternative treatment methods need to be explored. Compared to imaging measurement of tumor size which can lack sensitivity, and provide delayed indications of positive therapy response only, molecular tracking can provide more specific and up-to-date evaluation of treatment response[54]. Due to the rapid and minimally invasive nature of micro-histotripsy paired FNA, molecular evaluations of cancer response to therapy could theoretically be performed as frequently as needed. In order to extend the capabilities of FNA, shock-scattering micro-histotripsy is able to liquefy solid tumor tissue, and consequently facilitates aspiration of a larger and more consistent quantity of cellular material through fine needle for molecular and cytopathology analysis.

Our shock-scattering micro-histotripsy paired FNA technique is a promising candidate for augmenting conventional FNA, and we expect that such a technique would be relatively cost-effective. Apart from an initial investment of capital equipment for micro-histotripsy, the procedure itself should not cost any more than current FNAB if used for cytological analysis. Additional molecular testing via qPCR would cost around the order of a molecular COVID test (less than $20 USD). On the other hand, whole-genome sequencing would be significantly more expensive to perform and would certainly increase the cost and complexity, but would likely only be applied post-diagnosis for tumor characterization and establishment of personalized treatment.

Though our work with shock-scattering micro-histotripsy paired FNA shows promise in *in vivo* cancer models, we recognize that further studies must be performed for this technique to be clinically applicable. Our current study focused on a single DNA epimutation biomarker as a proof of concept, but hypermethylation of one gene alone may not confirm the presence of cancer. Further work to determine a suitable panel of multiple biomarkers, potentially made up of both gene mutations and epimutations, will be necessary for cancer diagnostics with high confidence.

Additionally, the post-procedural effects of shock-scattering micro-histotripsy on the patient, such as the potential for inflammation, edema, immune responses, or tumor modulation would have to be assessed more in-depth. Our study did follow mice through three micro-histotripsy treatments over the course of three weeks, with no signs of inflammation or mouse discomfort upon successful on-target histotripsy treatments, either immediately after treatment or in the days following. Quantifying these characteristics was not a focus of this study, and more substantial investigation would be needed. However, it is worth noting that in comparison, shock-scattering micro-histotripsy produces damage zones that are hundreds of times smaller than a single core needle biopsy core, and core needle biopsies also cause many side effects such as swelling, infection, and bleeding at a high rate[3]. While histotripsy ablation of cells resulting in release of various cytokines may be expected to produce some level of change in tumor gene expression as shown by some studies [55], this would not be expected to impact the accuracy of MH+FNAB for molecular analysis. The majority of aspirated material is acellular, the sample is acquired within 5 minutes of treatment, and the small scale of tumor ablation (around 1% of the tumor) may not produce an appreciable effect on tumor gene expression. Any potential changes in gene expression would be expected to occur in the range of multiple minutes to hours for rapid responses, and in the range of days for changes in development and pathogenesis[56], but additional studies are needed to determine longer-term impact of micro-histotripsy on the residual tumor in the living subject.

Currently, the shock-scattering micro-histotripsy transducers our technique uses are not designed for deep-tumor applications and can only achieve focal depths of up to 7mm. Other prototypes not used in this study have demonstrated focal depths of 2 cm, which may be sufficient for human clinical use in superficial regions such as breast, skin, and head and neck tumors. Ongoing work aims to develop improved transducers with steerable foci and greater histotripsy focal depths. Furthermore, our group has

recently developed an improved design for producing histotripsy at the tip of a fine needle, which has, so far, been presented at conferences[57]. By laterally actuating a needle produce flexural modes, cavitation can be produced at the needle tip without the need for an external transducer. This significantly increases potential treatment depth while maintaining a compact design, and may reduce concerns about suitable acoustic windows for histotripsy. Initial studies of this design use 25-gauge needles 1.5 inch (3.81 cm) in length, but pilot tests indicate that cavitation with longer needle lengths is possible.

Concerns have been noted around the possibility of micro-histotripsy liquefaction of cancer cells resulting in the dislodging and release of invasive cells into the bloodstream, turning them into circulating tumor cells. More extensive, targeted studies for investigating this concern will be required before micro-histotripsy paired FNA for cancer diagnosis can be used in a clinical context. However, multiple related studies on the effects of histotripsy on secondary malignancies and immune system response to cancer have produced no contraindications that would suggest an increased risk of metastasis arising from histotripsy treatment. Contrary to initial concerns, various studies on the immunological and abscopal effects of histotripsy for cancer conclude that partial histotripsy ablation of primary tumors is able to stimulate the immune system to not only target and destroy the primary tumor, but also reduce and resist the formation of metastatic lesions[38, 35]. While we cannot be sure that such immune effects apply in the case of micro-histotripsy, with such a small percentage of the tumor being ablated, it would also stand to reason that the overall disturbance and movement of cells would be minimal. It would, however, be worthwhile to perform studies in which mice treated with micro-histotripsy paired FNA are tracked for tumor progression and potential metastasis over a long period of time compared to a tumor-bearing untreated control.

While our design for targeting and alignment of histotripsy to the tumors is currently rudimentary, this study was designed for proof-of-concept in mice, and did not yet attempt to incorporate advanced targeting. Systems intended for larger mammals such as in pig models and eventually human subjects, would require different placement of devices and probes with more advanced targeting. While our study did not employ a quantitative targeting method, we would aim to have future iterations of our device have more advanced targeting options, such as motorized XYZ stereotactic positioning. For a higher-flexibility approach, it may also be possible to design an apparatus in which the histotripsy transducer has a clip-on attachment to an imaging probe, similar in design to the FUJIFILM Sonosite needle guides. This approach would allow clinicians to have the option for free-hand imaging guidance of micro-histotripsy.

Here, we have shown one potential micro-histotripsy treatment regimen with settings which allowed for successful, precise treatment of nano-liter volumes of tumor in mice models *in-vivo*. However our exploration of histotripsy pulse parameters and treatment duration, and associated effects on tumor treatment efficacy, were limited.

For clinical translation of this method to be possible, further refinement of the micro-histotripsy, optimizing for cavitation stability, precision, and quality of material for downstream analysis is crucial.

Histotripsy parameters such as pulse repetition frequency and pulse cycle number would be expected to alter the characteristics of the cavitation cloud which can affect both cavitation stability and ablation precision. Work by Simon *et al.* (2024)[58] established that higher PRFs allow cavitation to occur at significantly lower pressure thresholds. However, the total cavitation cloud area was also observed to increase with increasing PRF, with the potential to produce larger and more uncontrolled ablation areas. Additionally, increasing the number of N cycles per pulse has been shown to slightly increase the lateral width of the cavitation cloud slightly [59], as well as produce higher peak-negative pressures due to the shock-scattering effect [60].

While stiffer tissues can be resistant to histotripsy fractionation via shock-scattering at sub-intrinsic threshold pressures [61], studies have shown that the intrinsic threshold of cavitation for tissues is independent of stiffness for Young's moduli ¡ 1 MPa, and is around 25 - 30 MPa for most tissues [62]. Although the histotripsy used in MH+FNAB is shock-scattering histotripsy, our micro-histotripsy transducer is able to produce peak negative pressures up to 40 MPa with the current histotripsy settings, and thus we expect that slight changes in acoustic properties due to differences in tissue type, at shallow treatment depths, would not impact the efficacy of histotripsy treatment with our device. If the micro-histotripsy transducer were to be designed for deeper tissue penetration, it is likely that the effects of limited acoustic access windows and acoustic aberration due to tissue heterogeneity would intensify.

For the purposes of genetic analysis via qPCR, it is unlikely that there would be concern of over-treatment of histotripsy. In some pilot experiments (not reported), histotripsy applied for up to 10 minutes did not negatively affect the ability to perform molecular analysis on the sample via qPCR. Considering the qPCR target amplicons are all around 100-150 bps in length, it would make sense that any mechanical fractionation of DNA or mRNA would result in segments well above the lengths needed to detect the qPCR targets.

However, for the purposes of cytology and whole-genome sequencing, there is a valid concern that over-treatment past a certain point may fractionate cells and DNA to a point where the quality of material for analysis is affected. Whole-genome sequencing would likely be affected less, as one of the steps for preparation of DNA libraries for sequencing is to enzymatically fragment the DNA. Our work shows some support for this assumption, as fragmentation of the DNA in our histotripsy sample was observed in a DNA gel (Supplementary Fig. 3), but the DNA was still of sufficient quality and quantity for sequencing. For the use of MH+FNAB for cytology, it would be reasonable to expect that after a certain treatment duration, cells would be fractionated too much for cytological evaluation. With the current method of treating tumors for 3 minutes, we already observe a high quantity of acellular debris and acellular nuclei present in the cell smears.

In these cases, shortening the duration of treatment may improve the quality of samples for cytology and sequencing. Previous work by Landry *et al.* (2022)[63], using the same base transducer design in rat brains, achieved complete target ablation with a 10 second treatment time, albeit in brain, a much softer tissue. Considering this, the treatment time for MH+FNAB can certainly stand to be reduced without significant risk of incomplete ablation. However, if under-treatment were to become an issue, the primary concern would only be that tissues do not become fractionated enough for FNA, and larger tissue chunks may clog the needle and interfere with adequate sample collection. We have found experimentally that a 3-minute treatment time in soft tissue works to enable application of all three analysis methods used in this study, however future work could further optimize the time needed to perform the procedure in the clinic while ensuring maximum results for the chosen analysis method.

When using the micro-histotripsy transducers over the span of multiple experiments over multiple weeks of use, we have observed progressive increase in the threshold driving voltage for cavitation to occur, with minimal effect on cavitation cloud size as long as cavitation thresholds were achieved. We did not expressly explore micro-histotripsy cavitation reproducibility over time in this study. However, for clinical translatability, further investigation would need to be performed to elucidate the effects of transducer degradation on cavitation quality. It is recommended to check cavitation thresholds in tissue-mimicking media periodically to ensure micro-histotripsy transducer operation.

Truly relevant measures of pain from MH+FNAB treatment can only be assessed in human clinical trials, however, there is a strong possibility that MH+FNAB on surface-level tissues could be performed with only local anesthesia. Currently, all existing human clinical trials of histotripsy relate to mass debulking of tissue, and require performance under general anesthesia[31]. Such applications not only produce greater damage effects on targeted tissue, producing potential for greater procedural pain, but also require treatment times of over 30 minutes which necessitates general anesthesia to avoid patient movement. In contrast, micro-histotripsy produces damage on the level of a pin prick, and tissue liquefaction is achieved in 3 minutes although a treatment time under 1 minute is likely sufficient. Additionally, while the option for local anesthesia is variable, many conventional FNAB procedures such as those in the thyroid already use local anesthesia either topically or via subcutaneous injection[64]. Thus, administration of local anesthesia for MH+FNAB would not add to the procedural complexity beyond that of conventional methods.

A advanced application of shock-scattering micro-histotripsy for molecular characterization and diagnosis of cancer has been achieved with this work. This is also only the second of any kind of histotripsy to be explored for use in biomarker-based biopsies, and our work features by far the largest fold-enhancement of biomarkers compared to similar previous studies. This breakthrough research provides a methodology to augment current FNAB techniques which have been limited in their applications due to limitations in adequate sample acquisition and requirements for the presence of an experienced cytology specialist. Our method of implementing shock-scattering micro-histotripsy to enhance conventional FNA addresses the major limitations of FNA while

maintaining the minimally invasive benefits that have established FNA as a staple diagnostic procedure in many conditions. The shock-scattering micro-histotripsy system we use features ultrasound imaging guidance platforms which are already widely clinically utilized, and the custom micro-histotripsy transducer and driver system are compact enough to be simple add-ons to a fine-needle syringe. Compared to other histotripsy systems which require large machinery, large transducer arrays, and often sparsely available imaging platforms such as MRI, our proposed method simplifies potential integration into the clinical setting.

Shock-scattering micro-histotripsy paired fine-needle aspiration could change the way that cancer is diagnosed, treated, and tracked. Our approach shows promise for filling the gaps in the current standard of care to provide faster and more personalized treatment which may vastly improve patient outcomes.

4 Methods

4.1 Ultrasound and Histotripsy System Specifications

Histotripsy was applied using a custom single element piezoelectric shock-scattering micro-histotripsy transducer with a 7-mm focal length that produces a sub-millimeter focal zone. The custom micro-histotripsy transducer and driver board were developed in the lab group of Dr. Jeremy A. Brown (Dalhousie University). Unlike most current transducers for cavitational histotripsy which are large, multi-element arrays[65, 66, 36, 67], our custom transducer is a small, single-element transducer only 10 mm in diameter and is compact enough to be a simple add-on to a fine-needle syringe as shown in Fig. 2. The micro-histotripsy transducer features a centered 25-gauge needle through-hole for needle guidance. It features an air-backed 1-3 piezoelectric composite made of PZT-5A / epoxy bonded to an aluminum acoustic lens and a $\frac{1}{4}$ wavelength parylene matching layer[68]. The custom driver board features a high-voltage pulse generator circuit based on a design described by Brown and Lockwood (2002)[69]. Transmit control was achieved using a function generator connected to the driver board which was set to transmit at 6.3 MHz for 10 cycles per pulse at a pulse repetition rate of 1 kHz with an amplitude of 5.0 Vpp as shown in Fig. 2. Our micro-histotripsy transducer, which was previously characterized by Landry *et al.*, produces an estimated peak negative pressure of 40 MPa when driven at -350 VDC with 10-cycle pulses [63]. With an approximate acoustic attenuation of 0.47dB/mm in soft tissue for our 6.3 MHz acoustic frequency transducer, peak-negative pressures at 5mm tissue depth *in-vivo* would be around 30.5 MPa. Shock-scattering micro-histotripsy cavitation running on a -350 VDC power source for 3 minutes produces complete liquification of the targeted tissue area. Simultaneous ultrasound imaging guidance was performed using the Vevo 3100 (VisualSonics) equipped with a 40 MHz centered imaging transducer, as well as pre-histotripsy photoacoustic imaging for alignment. Both the ultrasound imaging transducer and the histotripsy transducer were secured in an orthogonal orientation using a custom 3D-printed holder. Variable positioning of the histotripsy transducer within the holder allowed for a range of treatment depths

up to 7mm below the surface of the skin. The ultrasound imaging probe with custom holder attachment was fixed to a stereotactic positioning frame included with the Vevo3100 Ultrasound System (Visualsonics) for fine control and positioning of the apparatus throughout the treatment duration.

4.2 Cell Line and Biomarker Selection

Breast cancer model cell lines were used to test and develop our histotripsy-coupled biopsy method. HCC-38 (CRL-2314, ATCC) and MCF-7 (HTB-22, ATCC) were chosen as triple negative and luminal human breast cancer cell lines respectively. HCC-38 was chosen for its known hypermethylation state of the BRCA1 gene promoter region, an epimutation that is a strong indicator of hereditary breast cancer risk [47]. Mouse melanoma cell lines YUMM1.G1 (CRL-3363, ATCC) containing the human-relevant BRAFV600E driver mutation[70], and B16F10 (CRL-6475, ATCC) with high melanin production for visualization were used for gene sequencing and cytology/histology imaging.

4.3 Mouse Models and Tumor Xenografts

SCID Hairless Outbred (SHO, Charles River), female mice at 11-40 weeks of age were used in this study. Flank tumor models were prepared in SHO mice from grafts of each of the following cancer cell lines. MCF-7 or HCC-38 were injected at 5 million cells per injection for the breast cancer xenograft model and YUMM1.G1 or B16F10 were injected at 1 million cells per injection for the melanoma allograft model in both flanks of the mice. Injections were composed of a 1:1 mixture of cells suspended in PBS and Matrigel matrix (Corning 356234) to a total injection volume of 100 µL per flank. Tumors were allowed to grow for 3-4 weeks or until at least 6 mm in diameter, with a humane endpoint set for tumors growing beyond 1 cm in diameter. Mice were housed in the following conditions: dark/light cycle is set on 12h/12h, ambient temperature range is 19 to 20 degrees Celsius, humidity 40-70%.

4.4 Histotripsy biomarker release from cancer cell line pellets

HCC-38 human breast cancer cells were grown to 80% confluency in a 175 cm^2 tissue culture flask. Cells were harvested by incubation in 1 mL 0.25% trypsin-EDTA solution for 5 minutes at 37°C. Detached cells were then resuspended in sterile PBS and centrifuged at $500 \times g$ for 5 minutes to pellet cells. The resulting cell pellet contained approximately 10 million cells and occupied the bottom 3 mm of a standard 50 mL conical centrifuge tube. The custom micro-histotripsy transducer was secured to a series of optical breadboard posts with translating micrometers in two orthogonal directions for precise movement and consistent holding position of the transducer relative to the cell pellet.

The custom histotripsy driver and transducer system was calibrated for cavitation in degassed deionized water to establish the minimum settings required to achieve ultrasound cavitation. Initial tests in water and PBS determined a minimum set-point of -120 VDC on the power supply to achieve a sustained cavitation bubble cloud. An

upper limit of -200 VDC was chosen to avoid over-voltage damage to the transducer and driver board electronics. Voltage set-points between -120 VDC and -200 VDC were sufficient to produce strong and consistent ultrasound cavitation, marked by an audible buzzing sound and a sub-milimeter sized white bubble cloud visible to the naked eye in the liquid medium. A set-point of -160 VDC was selected for all subsequent cell pellet experiments. To establish a baseline for the pre-histotripsy sample, rather than use the culture media that was in the flask, the cell pellets were washed in 2mL PBS three times, then pelleted one final time before taking a 500 µL sample of PBS supernatant from the top. Histotripsy was applied for varying times of 10, 30, 60, and 120 seconds in a fresh vial of cells each time. We also tested multi-area targeting in a separate group of samples, with changing of the focal spot 4 times for 3, 10, and 20 seconds per spot over the duration of the treatment. After each histotripsy application, the sample was centrifuged to pellet cells and cellular debris and a 500 µL sample of the PBS supernatant was extracted. Samples were analyzed for the cancer-specific BRCA1 hypermethylation marker via qPCR.

4.5 Histotripsy biomarker release from subcutaneously-injected tumors in mice

Fine needle aspiration biopsies both pre- and post-histotripsy were taken using a 25-gauge needle attached to a 1 mL syringe. Due to the extremely small volume of liquid or tissue that can be collected via fine needle (less than 20 µL), there was concern that the sample could be lost to the dead space in the needle and syringe, therefore the needle head was pre-loaded with 100 µL of 0.5M EDTA in water for the sample to dilute into. To allow for uninterrupted imaging and histotripsy, mice were anesthetized to surgical plane with 2% isoflurane in oxygen delivered at 1 L/min into an anesthesia chamber and then transferred onto a heated imaging platform for the remainder of the procedure.

The ultrasound imaging probe and histotripsy transducer is acoustically coupled to the mouse with warmed, degassed ultrasound gel. The gel is degassed by filling into 50 mL syringes and centrifuging at 500 × g for at least 20 minutes until no bubbles remain in order to prevent air from interfering with histotripsy cavitation. To identify the location of the histotripsy focal zone within the imaging field for alignment to the tumor, histotripsy and imaging transducers were first fixed in place, then ultrasound gel was applied on the surface of the histotripsy transducer, filling the gap between it and the imaging transducer. Away from the mouse, histotripsy was turned on to cavitate in gel for a few seconds in order for the operator to note the coordinates of the cavitation bubble in the B-mode imaging plane. The cavitation location in the imaging field was then aligned with the desired target location in the mouse tumor. Under ultrasound imaging, a pre-histotripsy fine-needle biopsy was taken in a chosen area of the tumor. This was performed using the needle through-hole in the custom histotripsy transducer for the purpose of consistency in comparison with post-histotripsy fine-needle aspiration method. The needle tip was inserted into the tumor until clearly visible under ultrasound, then constant negative pressure was applied for at least 1

minute by pulling all the way back on the syringe plunger along with careful rotational and axial movement of the needle.

A different area of the tumor was chosen for histotripsy application, and following the 3-minute histotripsy, a post-histotripsy fine-needle biopsy to aspirate the resulting liquified tissue was performed. The 3-minute histotripsy sonication time was chosen for being a sufficient length of time to completely liquefy various tissue including mouse tumor, liver, and muscle, based on visualization of liquid cavity in the tissue under ultrasound. The needle tip was inserted through the through-hole in the histotripsy transducer to align directly with the histotripsy-produced cavity, and pushed into the tumor until the needle tip was seen to come into contact with the histotripsy-produced cavity under ultrasound imaging. Negative pressure was applied by pulling the plunger for up to 1 minute or until red/pink fluid was seen diffusing into the EDTA solution in the needle head. All samples were dispensed into EDTA coated blood collection tubes and placed on ice and then stored in a -80°C freezer as soon as possible for downstream DNA/RNA extraction. Multiple freeze-thaw cycles of the samples were avoided to prevent degradation of nucleic acids.

A set of control conventional FNA experiments were performed by a trained cytopathologist. HCC-38 and B16F10 flank tumors were grown in 3 mice each, using the same methods as in above subsection Mouse Models and Tumor Xenografts. Once tumors had grown to size, the cytopathologist was asked to perform FNAB in-vivo on the tumor-bearing mice with whichever method they deemed appropriate. In this case, the cytopathologist chose to perform FNAB under ultrasound guidance using the pencil-grip method due to the small size of the tumors. Conventional FNA samples from B16F10 tumors were made into cell smears and FFPE cell pellet sections for cytopathology, while FNA samples from HCC-38 tumors were analyzed by qPCR.

Histotripsy ablation volumes were quantified from ultrasound B-scans by manually segmenting the histotripsy cavitation region and assuming cylindrical symmetry.

4.6 Nucleic acid extraction

For preliminary *in-vitro* histotripsy experiments using cancer cell line pellets, DNA and RNA were extracted from samples using the QIAamp DNA Micro Kit (56304, Qiagen) for DNA extraction, and RNeasy Mini Kit (74104, Qiagen) for RNA extraction following the manufacturer recommended protocols.

For *in vivo* histotripsy experiments in mouse models, we tested and found that at very low sample volumes, the presence of blood in the sample prevents extraction of biomarkers using the Qiagen kits. We opted to instead use the Zymo Research Direct-zol™ DNA/RNA Miniprep Kit (R2080, Zymo) as it did not have this issue. Samples were lysed in TRIzol according to the kit protocol for liquid samples, and RNA and DNA were extracted. Due to high amounts of DNA loss from the column in the RNA elution step, 20 µL of the RNA eluate fraction was transferred into the final DNA eluate fraction. The DNA fraction was then treated with RNaseH to digest any RNA contamination.

DNA samples were treated by bisulfite conversion using the Epigentek BisulFlash DNA Modification Kit (P-1026-050, Epigentek) for methylation-specific qPCR. RNA samples were reverse transcribed to cDNA using a cDNA reverse transcription kit (4368814, Thermo Fisher Scientific).

4.7 qPCR analysis of DNA and RNA biomarkers

Quantitative PCR (QuantStudio 6 Flex Real-time PCR System, Applied Biosystems) amplification of promoter region hypermethylation of the BRCA1 gene was performed alongside known DNA concentration standards to quantify DNA epimutation biomarkers released by histotripsy. qPCR primers and probes compatible with the TaqMan assay system were custom designed to be complementary to the bisulfite-converted sequence of either the methylated or unmethylated allele of the BRCA1 promoter. Custom primer sequences for BRCA1 were designed based on previous literature which utilized qMSP to determine the methylation status of BRCA1 as a predictor of PARP-inhibitor therapy response[71]. Custom primers also had to be designed for the bisulfite-converted version of beta-actin to be used as a control. Mastermix without UNG (4440043, Thermo Fisher Scientific) was utilized for methylation-specific qPCR, as methylated cytosine is converted to uracil during bisulfite treatment and would be subject to UNG mediated degradation.

Cataloged TaqMan gene expression assays were used for qPCR detection of ER, PR, HER2, and beta-actin cDNA (Hs01046816_m1, Hs01556702_m1, Hs01001580_m1, Hs99999903_m1, Thermo Fisher Scientific), along with a UNG-containing PCR master mix (4440038, Thermo Fisher Scientific). All qPCR primers were validated on cell line lysate samples to ensure compatibility with the chosen cell lines prior to use in experiments. Custom qPCR primer and probe sequences used in this study are listed in Supplementary Table 1. QuantStudio Real-Time PCR Software (v1.3) was used to visualize and export qPCR data.

4.8 Cytopathology

Mouse melanoma tumors for cytopathology were grown in mice and treated with histotripsy following the same method as with breast cancer tumors for qPCR analysis. FNA samples were collected directly into 100 µL of pH 7.0 EDTA buffer pre-loaded into the syringe. 20 µL of sample was then smeared on a slide within an hour of sampling, left to air dry for 10 minutes, and fixed in methanol followed by rapid H&E staining. The remainder of the sample was centrifuged at 500 × g to pellet, embedded in 3% agar, then formalin fixed, paraffin embedded, and sectioned onto slides for standard H&E staining. Anti-S100A4 immunohistochemical staining was performed using the Anti-S100A4 primary antibody [EPR14639(2)] (ab197896, Abcam) at a 1:400 dilution.

Cell smears and cell pellet H&E slides were imaged at 40x magnification using the Aperio ScanScope Model CS slide scanning microscope. Slides containing smears and pellets from histotripsy aspirates as well as from conventional FNA performed by a cytopathologist were blinded and reviewed by 2 cytopathologists. Number of cells per FOV was used as a quantitative measure of slide quality. The average number of cells

per 40X field was determined over 10 fields by starting with the most cellular field, then counting 5 fields along the vertical axis and 5 fields along the horizontal axis. QuPath (v0.5.1) was used to view and save images of slides for cytology.

4.9 Library prep and sequencing

Whole tumor and histotripsy aspirate samples from YUMM1.G1 mouse melanoma allograft tumors in mice were analyzed via whole-genome sequencing. DNA was extracted using TRIzol reagent (15596026,Thermo Fisher Scientific), then quality checked by performing DNA gel electrophoresis to check for smeared bands. Extracted gDNA was treated with RNaseA (19101, Qiagen) and purified using DNA Clean & Concentrator-5 kit (D4013, Zymo).

Construction of Libraries

Library prep was done with the Illumina DNA Prep kit and Nextera DNA CD Indexes (20060060 and 20018708, Illumina) using 150 ng of gDNA. Library prep and DNA sequencing were performed as per manufacturer instructions. Sequencing was performed on the NextSeq500 using the NextSeq 500/550 Mid Output Kit v2.5 following a 150 cycles sequencing protocol which included in-instrument demultiplexing of libraries according to their barcodes (20024904, Illumina). PhiX Control v3 (110-3001, Illumina) was spiked in to serve as an internal sequencing control.

Bioinformatics

Quality-trimming was conducted using the fastq-mcf algorithm with a Q score threshold of 30 and a minimal length to retain sequences of 100 bp length. For variant calling, libraries were aligned using bwa to the mouse genome version GRCm39 [72], while duplicates were marked and removed using elPrep [73]. Variants were called with the HaplotypeCaller algorithm from the Genomic Analysis Toolkit (GATK) [74]. Variants were filtered with biopet-vcffilter [75], using a minimal sampling depth of 10 and a minimal quality score of 20. Allelic frequencies were extracted using in-house scripts. The bcftools [76] were used to split multiallelic variants (showing more than one alternative allele) into separate records, each representing a single allele. Indels (insertion and deletion variants) were left-aligned to the reference genome using bcftools to standardize positioning of variants along the genome. Mutations were annotated using the ANNOVAR annotation suite[77]. Reference sequences for mutations (mm10) were downloaded via ANNOVAR in refGene format and VCF files generated from our variant calling pipeline were converted to ANNOVAR format (.avinput). The actual annotation of genetic variants was conducted with script table_annovar.pl, specifically targeting gene-based information from refGene database [77]. The databases clinVar [78] and COSMIC [51] were used to screen for mutations of clinical relevance at the gene level (including melanoma-associated mutations).

Bar plots were generated with in-house R scripts using library ggplot2.

4.10 Statistical Analysis

All statistical analyses were performed in R software (version 4.3.2) unless otherwise specified. Two-sided Wilcoxon signed rank exact test was used for paired comparisons between two or more groups, and Wilcoxon rank sum test was used for unpaired comparisons. Bonferroni correction was applied to individual p-values where appropriate to adjust for multiple comparisons. Levels of statistical significance were denoted as follows: not significant or ns, $p > 0.05$; *, $p \leq 0.05$; **, $p \leq 0.01$; ***, $p \leq 0.001$.

4.11 Ethics Approval

Every experiment involving animals, human participants, or clinical samples have been carried out following a protocol approved by an ethical commission. Ethics approval

for all experimental protocols involving live mice in this study was received from the University of Alberta Animal Care and Use Committee - Health Sciences. All methods were carried out in accordance with the approved Animal Use Protocol No. 3982.

Data Availability

All data supporting the findings of this study have been deposited in the Figshare database, and can be accessed via the following: https://doi.org/10.6084/m9.figshare.30611120

Any additional requests for information can be directed to, and will be fulfilled by, the corresponding authors.

Code Availability

Codes were created in R software (version 4.3.2) for generation of figures and statistical analysis. R packages used include dplyr (v1.1.4), ggplot2 (v3.4.4), ggpubr (v0.6.0), ggsignif (v0.6.4), Hmisc (v5.1-1), and tidyr (v1.3.0). Codes are accessible and are provided as part of the source data, which can be accessed via: https://doi.org/10.6084/m9.figshare.30611120

References

[1] E. Łukasiewicz, A. Ziemiecka, W. Jakubowski, J. Vojinovic, M. Bogucevska, and K. Dobruch-Sobczak, "Fine-needle versus core-needle biopsy–which one to choose in preoperative assessment of focal lesions in the breasts? literature review," *Journal of ultrasonography*, vol. 17, no. 71, pp. 267–274, 2017.

[2] G. M. Tse and P.-H. Tan, "Diagnosing breast lesions by fine needle aspiration cytology or core biopsy: which is better?," *Breast cancer research and treatment*, vol. 123, pp. 1–8, 2010.

[3] K. Matsumoto, T. Satoh, S. Egawa, S. Shimura, S. Kuwao, and S. Baba, "Efficacy and morbidity of transrectal ultrasound-guided 12-core biopsy for detection of prostate cancer in japanese men," *International journal of urology*, vol. 12, no. 4, pp. 353–360, 2005.

[4] A. Witt, D. Yavuz, C. Walchetseder, H. Strohmer, and E. Kubista, "Preoperative core needle biopsy as an independent risk factor for wound infection after breast surgery," *Obstetrics & Gynecology*, vol. 101, no. 4, pp. 745–750, 2003.

[5] A. L. Chetlen, C. Kasales, J. Mack, S. Schetter, and J. Zhu, "Hematoma formation during breast core needle biopsy in women taking antithrombotic therapy," *American Journal of Roentgenology*, vol. 201, no. 1, pp. 215–222, 2013.

[6] H. Maseki, K. Jimbo, C. Watase, T. Murata, S. Shiino, S. Takayama, N. Yamamoto, K. Satomi, A. Maeshima, M. Yoshida, *et al.*, "Clinical significance of tumor cell seeding associated with needle biopsy in patients with breast cancer," *Asian Journal of Surgery*, vol. 46, no. 9, pp. 3700–3704, 2023.

[7] S. M. Ha, E. Y. Chae, J. H. Cha, H. J. Shin, W. J. Choi, and H. H. Kim, "Growing bi-rads category 3 lesions on follow-up breast ultrasound: malignancy rates and worrisome features," *The British Journal of Radiology*, vol. 91, no. 1087, p. 20170787, 2018.

[8] J. K. Baum, L. G. Hanna, S. Acharyya, M. C. Mahoney, E. F. Conant, L. W. Bassett, and E. D. Pisano, "Use of bi-rads 3–probably benign category in the american college of radiology imaging network digital mammographic imaging screening trial," *Radiology*, vol. 260, no. 1, pp. 61–67, 2011.

[9] S.-M. Vimpeli, I. Saarenmaa, H. Huhtala, and S. Soimakallio, "Large-core needle biopsy versus fine-needle aspiration biopsy in solid breast lesions: comparison of costs and diagnostic value," *Acta Radiologica*, vol. 49, no. 8, pp. 863–869, 2008.

[10] S. Nagar, A. Iacco, T. Riggs, W. Kestenberg, and R. Keidan, "An analysis of fine needle aspiration versus core needle biopsy in clinically palpable breast lesions: a report on the predictive values and a cost comparison," *The American journal of surgery*, vol. 204, no. 2, pp. 193–198, 2012.

[11] J. P. Bulte, L. Polman, M. Schlooz-Vries, A. Werner, R. Besselink, K. Sessink, R. Mus, S. Lardenoije, M. Imhof-Tas, J. Bulten, *et al.*, "One-day core needle biopsy in a breast clinic: 4 years experience," *Breast cancer research and treatment*, vol. 137, pp. 609–616, 2013.

[12] M. C. Benson, "Fine-needle aspiration of the prostate," *NCI monogr*, vol. 7, pp. 19–24, 1988.

[13] A. A. Renshaw, A. Powell, J. Caso, and E. W. Gould, "Needle track seeding in renal mass biopsies," *Cancer Cytopathology*, vol. 127, no. 6, pp. 358–361, 2019.

[14] M. Wang, X. He, Y. Chang, G. Sun, and L. Thabane, "A sensitivity and specificity comparison of fine needle aspiration cytology and core needle biopsy in evaluation of suspicious breast lesions: A systematic review and meta-analysis," *The breast*, vol. 31, pp. 157–166, 2017.

[15] L. Lodewijk, M. R. Vriens, W. M. Vorselaars, N. T. van der Meij, J. W. Kist, M. W. Barentsz, H. M. Verkooijen, I. H. B. Rinkes, and G. D. Valk, "Same-day fine-needle aspiration cytology diagnosis for thyroid nodules achieves rapid anxiety decrease and high diagnostic accuracy," *Endocrine Practice*, vol. 22, no. 5, pp. 561–566, 2016.

[16] A. Ly, J. C. Ono, K. S. Hughes, M. B. Pitman, and R. Balassanian, "Fine-needle aspiration biopsy of palpable breast masses: patterns of clinical use and patient experience," *Journal of the National Comprehensive Cancer Network*, vol. 14,

no. 5, pp. 527–536, 2016.

[17] A. Nassar, "Core needle biopsy versus fine needle aspiration biopsy in breast—a historical perspective and opportunities in the modern era," *Diagnostic cytopathology*, vol. 39, no. 5, pp. 380–388, 2011.

[18] P. Britton, "Fine needle aspiration or core biopsy," *The Breast*, vol. 8, no. 1, pp. 1–4, 1999.

[19] G. Gomez-Macias, R. Garza-Guajardo, J. Segura-Luna, and O. Barboza-Quintana, "Inadequate fine needle aspiration biopsy samples: pathologists versus other specialists," *Cytojournal*, vol. 6, 2009.

[20] M. Ghofrani, D. Beckman, and D. L. Rimm, "The value of onsite adequacy assessment of thyroid fine-needle aspirations is a function of operator experience," *Cancer Cytopathology: Interdisciplinary International Journal of the American Cancer Society*, vol. 108, no. 2, pp. 110–113, 2006.

[21] S. Perakis and M. R. Speicher, "Emerging concepts in liquid biopsies," *BMC medicine*, vol. 15, pp. 1–12, 2017.

[22] S. N. Lone, S. Nisar, T. Masoodi, M. Singh, A. Rizwan, S. Hashem, W. El-Rifai, D. Bedognetti, S. K. Batra, M. Haris, *et al.*, "Liquid biopsy: a step closer to transform diagnosis, prognosis and future of cancer treatments," *Molecular cancer*, vol. 21, no. 1, p. 79, 2022.

[23] A. L. D'Souza, J. R. Tseng, K. B. Pauly, S. Guccione, J. Rosenberg, S. S. Gambhir, and G. M. Glazer, "A strategy for blood biomarker amplification and localization using ultrasound," *Proceedings of the National Academy of Sciences*, vol. 106, no. 40, pp. 17152–17157, 2009.

[24] A. Forbrich, R. Paproski, M. Hitt, and R. Zemp, "Microbubble-enhanced ultrasound liberation of mrna biomarkers in vitro," *Ultrasound in medicine & biology*, vol. 39, no. 6, pp. 1087–1093, 2013.

[25] A. Forbrich, R. Paproski, M. Hitt, and R. Zemp, "Comparing efficiency of micro-rna and mrna biomarker liberation with microbubble-enhanced ultrasound exposure," *Ultrasound in Medicine & Biology*, vol. 40, no. 9, pp. 2207–2216, 2014.

[26] R. J. Paproski, A. Forbrich, M. Hitt, and R. Zemp, "Rna biomarker release with ultrasound and phase-change nanodroplets," *Ultrasound in Medicine & Biology*, vol. 40, no. 8, pp. 1847–1856, 2014.

[27] R. J. Paproski, J. Jovel, G. K.-S. Wong, J. D. Lewis, and R. J. Zemp, "Enhanced detection of cancer biomarkers in blood-borne extracellular vesicles using nanodroplets and focused ultrasound," *Cancer Research*, vol. 77, no. 1, pp. 3–13, 2017.

[28] J. Yuan, L. Xu, C.-Y. Chien, Y. Yang, Y. Yue, S. Fadera, A. H. Stark, K. E. Schwetye, A. Nazeri, R. Desai, *et al.*, "First-in-human prospective trial of sonobiopsy in high-grade glioma patients using neuronavigation-guided focused ultrasound," *NPJ Precision Oncology*, vol. 7, no. 1, p. 92, 2023.

[29] K. B. Bader, E. Vlaisavljevich, and A. D. Maxwell, "For whom the bubble grows: physical principles of bubble nucleation and dynamics in histotripsy ultrasound therapy," *Ultrasound in medicine & biology*, vol. 45, no. 5, pp. 1056–1080, 2019.

[30] E. Vlaisavljevich, A. Maxwell, L. Mancia, E. Johnsen, C. Cain, and Z. Xu, "Visualizing the histotripsy process: Bubble cloud–cancer cell interactions in a

tissue-mimicking environment," *Ultrasound in medicine & biology*, vol. 42, no. 10, pp. 2466–2477, 2016.

[31] Z. Xu, T. D. Khokhlova, C. S. Cho, and V. A. Khokhlova, "Histotripsy: a method for mechanical tissue ablation with ultrasound," *Annual Review of Biomedical Engineering*, vol. 26, 2024.

[32] R. P. Williams, J. C. Simon, V. A. Khokhlova, O. A. Sapozhnikov, and T. D. Khokhlova, "The histotripsy spectrum: differences and similarities in techniques and instrumentation," *International Journal of Hyperthermia*, vol. 40, no. 1, p. 2233720, 2023.

[33] Z. Xu, T. L. Hall, E. Vlaisavljevich, and F. T. Lee Jr, "Histotripsy: the first noninvasive, non-ionizing, non-thermal ablation technique based on ultrasound," *International Journal of Hyperthermia*, vol. 38, no. 1, pp. 561–575, 2021.

[34] X. Zhang, G. E. Owens, H. S. Gurm, Y. Ding, C. A. Cain, and Z. Xu, "Noninvasive thrombolysis using histotripsy beyond the intrinsic threshold (microtripsy)," *IEEE transactions on ultrasonics, ferroelectrics, and frequency control*, vol. 62, no. 7, pp. 1342–1355, 2015.

[35] T. Worlikar, M. Zhang, A. Ganguly, T. L. Hall, J. Shi, L. Zhao, F. T. Lee, M. Mendiratta-Lala, C. S. Cho, and Z. Xu, "Impact of histotripsy on development of intrahepatic metastases in a rodent liver tumor model," *Cancers*, vol. 14, no. 7, p. 1612, 2022.

[36] E. Vlaisavljevich, Y. Kim, S. Allen, G. Owens, S. Pelletier, C. Cain, K. Ives, and Z. Xu, "Image-guided non-invasive ultrasound liver ablation using histotripsy: feasibility study in an in vivo porcine model," *Ultrasound in medicine & biology*, vol. 39, no. 8, pp. 1398–1409, 2013.

[37] G. R. Schade, J. Keller, K. Ives, X. Cheng, T. J. Rosol, E. Keller, and W. W. Roberts, "Histotripsy focal ablation of implanted prostate tumor in an ace-1 canine cancer model," *The Journal of urology*, vol. 188, no. 5, pp. 1957–1964, 2012.

[38] S. Qu, T. Worlikar, A. E. Felsted, A. Ganguly, M. V. Beems, R. Hubbard, A. L. Pepple, A. A. Kevelin, H. Garavaglia, J. Dib, *et al.*, "Non-thermal histotripsy tumor ablation promotes abscopal immune responses that enhance cancer immunotherapy," *Journal for immunotherapy of cancer*, vol. 8, no. 1, 2020.

[39] A. Hendricks-Wenger, P. Weber, A. Simon, S. Saunier, S. Coutermarsh-Ott, D. Grider, J. Vidal-Jové, I. C. Allen, D. Luyimbazi, and E. Vlaisavljevich, "Histotripsy for the treatment of cholangiocarcinoma liver tumors: In vivo feasibility and ex vivo dosimetry study," *IEEE transactions on ultrasonics, ferroelectrics, and frequency control*, vol. 68, no. 9, pp. 2953–2964, 2021.

[40] G. R. Schade, Y.-N. Wang, S. D'Andrea, J. H. Hwang, W. C. Liles, and T. D. Khokhlova, "Boiling histotripsy ablation of renal cell carcinoma in the eker rat promotes a systemic inflammatory response," *Ultrasound in medicine & biology*, vol. 45, no. 1, pp. 137–147, 2019.

[41] J. Gannon, K. M. Imran, A. Hendricks-Wenger, M. Edwards, H. Covell, L. Ruger, N. Singh, M. Nagai-Singer, B. Tintera, K. Eden, *et al.*, "Ultrasound-guided non-invasive pancreas ablation using histotripsy: feasibility study in an in vivo porcine model," *International Journal of Hyperthermia*, vol. 40, no. 1, p. 2247187, 2023.

[42] L. N. Ruger, A. N. Hay, J. M. Gannon, H. O. Sheppard, S. L. Coutermarsh-Ott, G. B. Daniel, K. R. Kierski, B. J. Ciepluch, E. Vlaisavljevich, and J. L. Tuohy, "Histotripsy ablation of spontaneously occurring canine bone tumors," *IEEE Transactions on Biomedical Engineering*, vol. 70, no. 1, pp. 331–342, 2022.

[43] S. W. Choi, S. Duclos, S. Camelo-Piragua, N. Chaudhary, J. Sukovich, T. Hall, A. Pandey, and Z. Xu, "Histotripsy treatment of murine brain and glioma: temporal profile of magnetic resonance imaging and histological characteristics post-treatment," *Ultrasound in medicine & biology*, vol. 49, no. 8, pp. 1882–1891, 2023.

[44] T. Worlikar, M. Mendiratta-Lala, E. Vlaisavljevich, R. Hubbard, J. Shi, T. L. Hall, C. S. Cho, F. T. Lee, J. Greve, and Z. Xu, "Effects of histotripsy on local tumor progression in an in vivo orthotopic rodent liver tumor model," *BME frontiers*, vol. 2020, 2020.

[45] J. R. Chevillet, T. D. Khokhlova, M. D. Giraldez, G. R. Schade, F. Starr, Y.-N. Wang, E. N. Gallichotte, K. Wang, J. H. Hwang, and M. Tewari, "Release of cell-free microrna tumor biomarkers into the blood circulation with pulsed focused ultrasound: A noninvasive, anatomically localized, molecular liquid biopsy," *Radiology*, vol. 283, no. 1, pp. 158–167, 2017.

[46] M. P. Lux, P. A. Fasching, and M. W. Beckmann, "Hereditary breast and ovarian cancer: review and future perspectives," *Journal of molecular medicine*, vol. 84, pp. 16–28, 2006.

[47] L. Zhang and X. Long, "Association of brca1 promoter methylation with sporadic breast cancers: Evidence from 40 studies," *Scientific reports*, vol. 5, no. 1, p. 17869, 2015.

[48] T. Nyberg, D. Frost, D. Barrowdale, D. G. Evans, E. Bancroft, J. Adlard, M. Ahmed, J. Barwell, A. F. Brady, C. Brewer, *et al.*, "Prostate cancer risks for male brca1 and brca2 mutation carriers: a prospective cohort study," *European urology*, vol. 77, no. 1, pp. 24–35, 2020.

[49] M. Srinivasan, D. Sedmak, and S. Jewell, "Effect of fixatives and tissue processing on the content and integrity of nucleic acids," *The American journal of pathology*, vol. 161, no. 6, pp. 1961–1971, 2002.

[50] S. Q. Wong, J. Li, A. Y. Tan, R. Vedururu, J.-M. B. Pang, H. Do, J. Ellul, K. Doig, A. Bell, G. A. McArthur, *et al.*, "Sequence artefacts in a prospective series of formalin-fixed tumours tested for mutations in hotspot regions by massively parallel sequencing," *BMC medical genomics*, vol. 7, no. 1, p. 23, 2014.

[51] J. G. Tate, S. Bamford, H. C. Jubb, Z. Sondka, D. M. Beare, N. Bindal, H. Boutselakis, C. G. Cole, C. Creatore, E. Dawson, *et al.*, "Cosmic: the catalogue of somatic mutations in cancer," *Nucleic acids research*, vol. 47, no. D1, pp. D941–D947, 2019.

[52] K. T. Flaherty, J. R. Infante, A. Daud, R. Gonzalez, R. F. Kefford, J. Sosman, O. Hamid, L. Schuchter, J. Cebon, N. Ibrahim, *et al.*, "Combined braf and mek inhibition in melanoma with braf v600 mutations," *New England Journal of Medicine*, vol. 367, no. 18, pp. 1694–1703, 2012.

[53] H. A. Domanski, "Role of fine needle aspiration cytology in the diagnosis of soft tissue tumours," *Cytopathology*, vol. 31, no. 4, pp. 271–279, 2020.

[54] A. A. Neves and K. M. Brindle, "Assessing responses to cancer therapy using molecular imaging," *Biochimica et Biophysica Acta (BBA)-Reviews on Cancer*, vol. 1766, no. 2, pp. 242–261, 2006.

[55] I. Iwanicki, L. L. Wu, F. Flores-Guzman, R. Sundland, P. Viza-Gomes, R. Nordgren, C. S. Centner, J. J. Kandel, M. A. Applebaum, K. B. Bader, *et al.*, "Histotripsy induces apoptosis and reduces hypoxia in a neuroblastoma xenograft model," *International Journal of Hyperthermia*, vol. 40, no. 1, p. 2222941, 2023.

[56] N. Yosef and A. Regev, "Impulse control: temporal dynamics in gene transcription," *Cell*, vol. 144, no. 6, pp. 886–896, 2011.

[57] E. McAlister, J. Wang, P. Kedarisetti, F. Wuest, and R. Zemp, "Needle tip histotripsy enables rapid, lamp-based, point-of-care cancer diagnostics [oral presentation]." International Ultrasonics Symposium, Utrecht, Netherlands, September 2025.

[58] A. Simon, C. Edsall, A. Maxwell, and E. Vlaisavljevich, "Effects of pulse repetition frequency on bubble cloud characteristics and ablation in single-cycle histotripsy," *Physics in Medicine & Biology*, vol. 69, no. 2, p. 025018, 2024.

[59] T. G. Landry and J. A. Brown, "Ultrasound imaging guided precision histotripsy: Effects of pulse settings on ablation properties in rat brain," *The Journal of the Acoustical Society of America*, vol. 155, no. 4, pp. 2860–2874, 2024.

[60] A. D. Maxwell, T.-Y. Wang, C. A. Cain, J. B. Fowlkes, O. A. Sapozhnikov, M. R. Bailey, and Z. Xu, "Cavitation clouds created by shock scattering from bubbles during histotripsy," *The Journal of the Acoustical Society of America*, vol. 130, no. 4, pp. 1888–1898, 2011.

[61] E. Vlaisavljevich, A. Maxwell, M. Warnez, E. Johnsen, C. A. Cain, and Z. Xu, "Histotripsy-induced cavitation cloud initiation thresholds in tissues of different mechanical properties," *IEEE transactions on ultrasonics, ferroelectrics, and frequency control*, vol. 61, no. 2, pp. 341–352, 2018.

[62] E. Vlaisavljevich, K.-W. Lin, A. Maxwell, M. T. Warnez, L. Mancia, R. Singh, A. J. Putnam, B. Fowlkes, E. Johnsen, C. Cain, *et al.*, "Effects of ultrasound frequency and tissue stiffness on the histotripsy intrinsic threshold for cavitation," *Ultrasound in medicine & biology*, vol. 41, no. 6, pp. 1651–1667, 2015.

[63] T. G. Landry, J. Gannon, E. Vlaisavljevich, M. G. Mallay, J. K. Woodacre, S. Croul, J. P. Fawcett, and J. A. Brown, "Endoscopic coregistered ultrasound imaging and precision histotripsy: Initial in vivo evaluation," *BME frontiers*, 2022.

[64] C. Cao, S. Jasim, A. Cherian, A. Nassar, A.-M. Chindris, A. M. Rivas, S. Bonnett, M. Caserta, M. N. Stan, and V. J. Bernet, "Patient discomfort in relation to thyroid nodule fine-needle aspiration (fna) performed with or without parenteral and/or topical anesthetic," *Endocrine Practice*, vol. 26, no. 12, pp. 1497–1504, 2020.

[65] T. D. Khokhlova, Y.-N. Wang, J. C. Simon, B. W. Cunitz, F. Starr, M. Paun, L. A. Crum, M. R. Bailey, and V. A. Khokhlova, "Ultrasound-guided tissue fractionation by high intensity focused ultrasound in an in vivo porcine liver model," *Proceedings of the National Academy of Sciences*, vol. 111, no. 22, pp. 8161–8166, 2014.

[66] T. D. Khokhlova, G. R. Schade, Y.-N. Wang, S. V. Buravkov, V. P. Chernikov,

J. C. Simon, F. Starr, A. D. Maxwell, M. R. Bailey, W. Kreider, *et al.*, "Pilot in vivo studies on transcutaneous boiling histotripsy in porcine liver and kidney," *Scientific reports*, vol. 9, no. 1, p. 20176, 2019.

[67] G. E. Stocker, J. E. Lundt, J. R. Sukovich, R. M. Miller, A. P. Duryea, T. L. Hall, and Z. Xu, "A modular, kerf-minimizing approach for therapeutic ultrasound phased array construction," *IEEE transactions on ultrasonics, ferroelectrics, and frequency control*, vol. 69, no. 10, pp. 2766–2775, 2022.

[68] J. K. Woodacre, T. G. Landry, and J. A. Brown, "A low-cost miniature histotripsy transducer for precision tissue ablation," *IEEE transactions on ultrasonics, ferroelectrics, and frequency control*, vol. 65, no. 11, pp. 2131–2140, 2018.

[69] J. A. Brown and G. R. Lockwood, "Low-cost, high-performance pulse generator for ultrasound imaging," *IEEE transactions on ultrasonics, ferroelectrics, and frequency control*, vol. 49, no. 6, pp. 848–851, 2002.

[70] K. Meeth, J. X. Wang, G. Micevic, W. Damsky, and M. W. Bosenberg, "The yumm lines: a series of congenic mouse melanoma cell lines with defined genetic alterations," *Pigment cell & melanoma research*, vol. 29, no. 5, pp. 590–597, 2016.

[71] I. Ibragimova and P. Cairns, "Assays for hypermethylation of the brca1 gene promoter in tumor cells to predict sensitivity to parp-inhibitor therapy," *Poly (ADP-Ribose) Polymerase: Methods and Protocols*, pp. 277–291, 2011.

[72] H. Li, "Aligning sequence reads, clone sequences and assembly contigs with bwa-mem," 2013.

[73] C. Herzeel, P. Costanza, D. Decap, J. Fostier, R. Wuyts, and W. Verachtert, "Multithreaded variant calling in elprep 5," *PLoS One*, vol. 16, no. 2, p. e0244471, 2021.

[74] G. A. Van der Auwera and B. D. O'Connor, "Genomics in the cloud: using docker, gatk, and wdl in terra," 2020.

[75] P. Van't Hof, W. Arindrarto, S. Bollen, S. Kielbasa, J. Laros, and H. Mei, "Biopet: towards scalable, maintainable, user-friendly, robust and flexible ngs data analysis pipelines," in *2017 17th IEEE/ACM International Symposium on Cluster, Cloud and Grid Computing (CCGRID)*, pp. 823–829, IEEE, 2017.

[76] H. Li, "A statistical framework for snp calling, mutation discovery, association mapping and population genetical parameter estimation from sequencing data," *Bioinformatics*, vol. 27, no. 21, pp. 2987–2993, 2011.

[77] K. Wang, M. Li, and H. Hakonarson, "Annovar: functional annotation of genetic variants from high-throughput sequencing data," *Nucleic acids research*, vol. 38, no. 16, pp. e164–e164, 2010.

[78] M. J. Landrum, J. M. Lee, G. R. Riley, W. Jang, W. S. Rubinstein, D. M. Church, and D. R. Maglott, "Clinvar: public archive of relationships among sequence variation and human phenotype," *Nucleic acids research*, vol. 42, no. D1, pp. D980–D985, 2014.

Acknowledgements

Funding: We gratefully acknowledge funding from the Alberta Cancer Foundation (ACF JFMRP 27587, RJZ), the Mary Johnston Chair for Melanoma Research (ACF

JFMRP 27587), an Alberta Cancer Research for Screening and Prevention Grant (CRSPPF 017061, RJZ), and the Canadian Cancer Society (CCS 702032, RJZ). PK (PGSD3-558531-2021), JW (CGSM 574839-2022) and EAM (CGSM 596784-2024) acknowledge scholarship funding from NSERC.

Author Contributions Statement

JW designed and performed experiments, performed photoacoustic and micro-ultrasound imaging, analyzed qPCR data, and wrote the manuscript. PK and EAM helped with qPCR, cell culture work, photoacoustic and ultrasound imaging, and helped write the manuscript. BAA and RJM analyzed cytopathology data and provided clinical guidance. JKW, MGM, and JAB designed, fabricated and tested the micro-histotripsy transducer and driving electronics. FRW supervised wet lab work, helped design the studies, and reviewed the manuscript. JJ performed bioinformatic analysis for whole genome sequencing, and wrote the section of the manuscript pertaining to it. RJZ designed and supervised the experiments and assisted in analyzing the data and writing the manuscript.

Competing Interests Statement

RJZ is a founder and shareholder of 5Q Laser Inc., OptoBiomeDx Inc., CliniSonix Inc., and IllumiSonics Inc., which however did not support this work. RJZ served on the Scientific Advisory Board of FUJIFILM Visualsonics, which, however, did not support this work. JW, PK, EAM, and FRW are shareholders of OptoBiomeDx Inc., which however did not support this work. JAB is a founder and shareholder of SoundBlade Medical Inc. and DaxSonics Inc., which, however, did not support this work. The histotripsy transducer and electronics are protected by patent (Daxsonics Ultrasound Inc., Jeffrey Kyle Woodacre and Jeremy Brown, US11806553B2, active status). The remaining authors declare no competing interests.

Figure Legends/Captions

Figure 1: Illustrations of current clinical standards of biopsy compared to our method of shock-scattering micro-histotripsy paired fine-needle aspiration biopsy. Portions of figure created in BioRender. Zemp, R. (2026) https://BioRender.com/yi8pn88, https://BioRender.com/mmtr3hq, https://BioRender.com/xhsqz77, https://BioRender.com/mt28456.

Figure 2: Micro-histotripsy system and transducer specifications and imaging setup. **(A)** Micro-histotripsy custom driver board connects to a -350 VDC power supply and is driven by a function generator set to cycle at 6.3 MHz with 10 cycles per transmit pulse at a pulse repetition frequency of 1-kHz. The transducer produces an estimated peak-negative pressure of 40 MPa in water, and around 30 MPa *in-vivo* due to attenuation. **(B)** Custom 1-3 piezoelectric composite micro-histotripsy transducer is 10 mm in diameter, small enough to be an easy add-on to the end of a fine needle. **(C)** Schematic of the positioning of imaging and histotripsy transducers, held

together by a custom 3D-printed holder, relative to a target tumor. **(D)** Photograph of the custom 3D-printed transducer holder. **(E)** Illustration of experimental method *in vivo* in a mouse model. Portions of figure created in BioRender. Zemp, R. (2026) https://BioRender.com/z3tcz3x, https://BioRender.com/c70v140.

Figure 3: Qualitative effects of shock-scattering micro-histotripsy cavitation on tumor tissue. **(A)** Ultrasound images showing mouse tumor during histotripsy, post-histotripsy liquid cavity, and FNA of liquid in histotripsy cavity. The dotted blue line indicates tumor boundary, and the dotted yellow line indicates the 25-gauge fine needle. **(B)** Oxygen-saturation PA imaging overlay on B-mode ultrasound of *in vivo* mouse tumor before and immediately post-histotripsy. Histotripsy ablation cavity is indicated by a yellow circle, and PA SNR for the area within the tumor boundary is shown for each respective image. **(C)** Excised mouse flank tumor following histotripsy treatment and euthanasia of the mouse. The tumor is sitting atop a No.21 surgical scalpel blade, and the tiny "hole" (blue arrow) from the histotripsy cavitation is visible on the face of the tumor. **(D)** H&E sections of adjacent (left) and on-target (right) slices of the same region of the same tumor treated by micro-histotripsy cavitation. Histotripsy produces a sharp boundary at the edge of the treatment zone without disturbing or affecting the morphology of the remaining tumor tissue in the surroundings. Yellow circle indicates region of histotripsy ablation. Red arrows show loosened cells and tissue likely to be aspirated into the sample.

Figure 4: Micro-histotripsy liquefaction of tumors enhances cancer-specific BRCA1 epimutation release. **(A)** Unmethylated and methylated alleles of BRCA1 promoter region were detected via qPCR in conventional FNA, pre-histotripsy FNA, or histotripsy+FNA samples (n=3 tumors conventional FNA, n=15 tumors pre-histotripsy, n=9 tumors MH+FNA). DNA copies detected are plotted on a log10 scale, error bars represent standard error. Both unmethylated and methylated alleles of the BRCA1 promoter region were significantly higher in the histotripsy+FNA group compared to the conventional FNA ($p = 0.00084$ and 0.00015, respectively) and pre-histotripsy FNA ($p = 0.0035$ and 4.58e-5, respectively) controls. There is no significant difference in BRCA1 biomarker detection between conventional and pre-histotripsy FNA samples ($p = 0.43$ for unmethylated allele and $p = 0.065$ for methylated allele). **(B)** Representative qPCR curves for pre-histotripsy FNA control and post-histotripsy FNA samples. Groups were compared using two-sided Wilcoxon signed rank exact test (paired comparisons) and two-sided Wilcoxon rank sum test (unpaired comparisons) with Bonferroni correction for multiple comparisons.*$P < 0.05$; **$P < 0.01$; ***$P < 0.001$; ns $P > 0.05$.

Figure 5: Micro-histotripsy liquefaction of tumors enhances cancer subtype-specific hormone receptor mRNA biomarker release. **(A)** ER, PR, and HER2 mRNA levels were quantified in conventional FNA, pre-histotripsy FNA, or histotripsy+FNA samples in a luminal breast cancer (ER/PR+) or TNBC cancer type (luminal n=8 pre-histotripsy, n=6 post-histotripsy; TNBC n=18 pre-histotripsy, n=11 post-histotripsy; samples in duplicate). mRNA copies detected are plotted on a log10 scale, error bars

represent standard error. ER and PR mRNA levels were significantly higher post-histotripsy versus control ($p = 0.048$ and 0.036, respectively) in the luminal subtype, while no difference was observed in the TNBC subtype ($p = 0.55$ and 0.61, respectively). HER2 mRNA levels were amplified post-histotripsy in the TNBC subtype ($p = 2.57e\text{-}4$) despite both cell types used being known HER2 negative subtypes. **(B)** Representative gene expression qPCR curves for pre-histotripsy FNA control and post-histotripsy FNA samples. **(C)** Control experiment against a true HER2+ cell line shows that the HER2- cancer types still amplify under qPCR due to primer sensitivity, but significantly less quantity of HER2 mRNA is detected compared to HER2+ control ($p = 0.0095$) (n=2 different cell lines each for HER2+ and HER2- groups, in triplicate). Groups were compared using two-sided Wilcoxon signed rank exact test (paired comparisons) and two-sided Wilcoxon rank sum test (unpaired comparisons) with Bonferroni correction for multiple comparisons. *$P < 0.05$; **$P < 0.01$; ***$P < 0.001$; ns $P > 0.05$.

Figure 6: Cell smears and sectioned cell pellet slides for cytology analysis. **(A)** Cell smears and FFPE sectioned cell pellet slide comparisons between conventional FNAB, pre-histotripsy FNA, and MH+FNAB, stained with H&E and anti-S100A4 immunohistochemistry. In the pre-histotripsy samples, minimal material for staining and imaging could be extracted even after 5 separate attempts on different mice. In the MH+FNAB samples, mostly loose cells can be seen with some cell clusters (CL), on a backdrop of acellular debris (cloudy pink material in H&E). Cells in the sample exhibit classic signs of malignancy like condensed chromatin and prominent nucleoli (red arrow) as well as melanin expression (*). Cells stain positive for S100A4 (yellow arrows), a standard protein biomarker in melanoma.**(B)** Pathologist-evaluated cell counts per 40X FOV, with pooled scores of 10 FOVs per slide, per pathologist. Two pathologists performed blinded slide reviews on n=12 FNA smears, n=2 histotripsy smears, n=6 FNA pellets, and n=1 histotripsy pellet slides.

Figure 7: Mouse melanoma tumor and matching histotripsy sample mutations along the chromosome. **(A)**(top) Mutations found within the genome of a YUMM1.G1 mouse melanoma flank tumor inoculated in a mouse model and (bottom) within the genome of a histotripsy lysate sample extracted via FNA from the same YUMM1.G1 tumor. **(B)** Tumor versus histotripsy lysate DNA mutations per million reads on a log10 scale. **(C)** Number of histotripsy lysate DNA mutations normalized to mutation count in the tumor genome.

Current Biopsy Procedures

Core Needle Biopsy

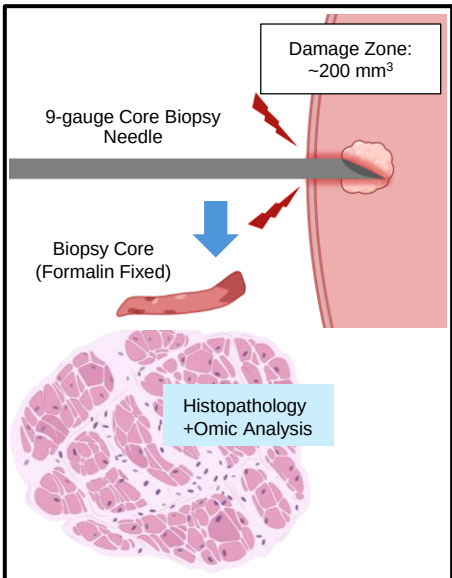

- \+ Gold Standard For Cancer Diagnosis
- \+ Lots Of Material Extracted
- − Painful
- − Risk of Infection
- − Can Not Be Performed Frequently
- − Poor Sequencing From Formalin-Fixation

Liquid Biopsy

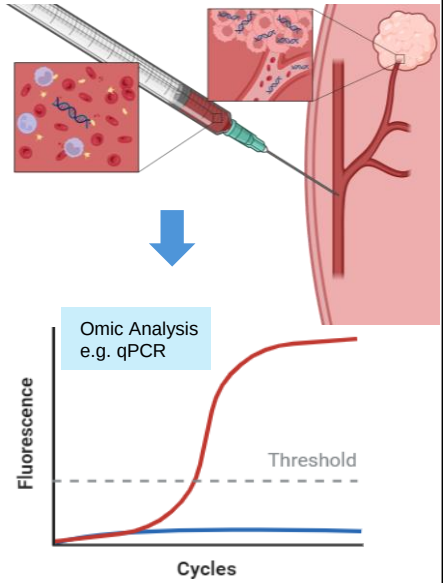

- \+ Least Invasive (i.e. Blood Draw)
- \+ Earlier Cancer Detection
- − Low Biomarkers
- − No Histo/Cytopathology
- − No Local Sampling Of Tumor Tissue

Fine Needle Aspiration Biopsy

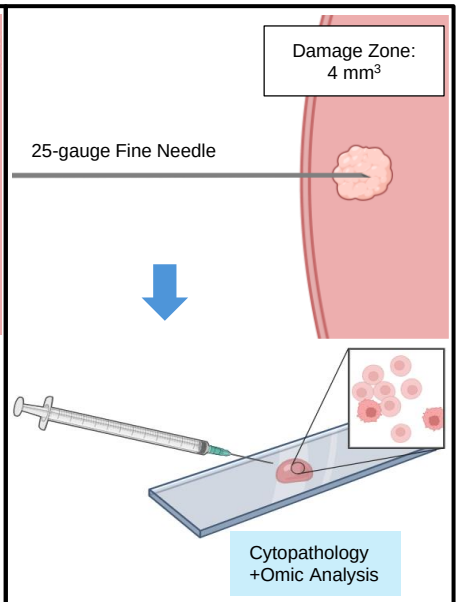

- \+ Less Invasive
- \+ Cytopathology Available
- − Minimal Material Extracted
- − Success Dependent on Clinician Experience
- − Questionable Sequencing Coverage

Our Method

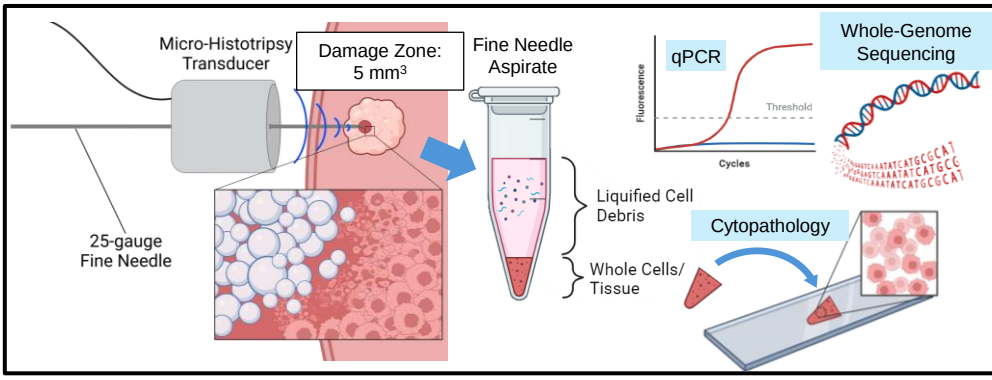

- \+ Less Invasive
- \+ Earlier Cancer Detection
- \+ Massive Biomarker Release
- \+ More Cell/Tissue Material
- \+ Direct Sampling Of Tumor Tissue
- − Minimal Intact Tissue Structure

A

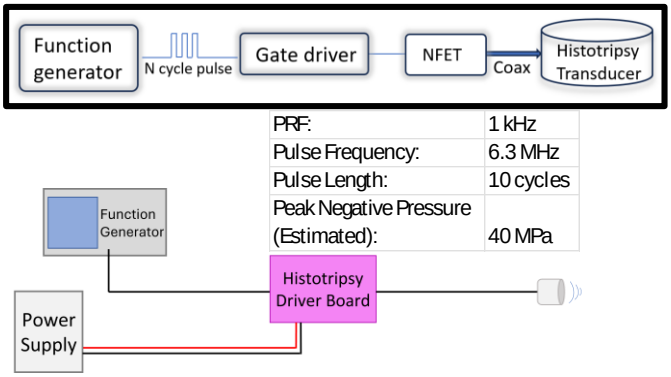

PRF:	1 kHz
Pulse Frequency:	6.3 MHz
Pulse Length:	10 cycles
Peak Negative Pressure (Estimated):	40 MPa

B

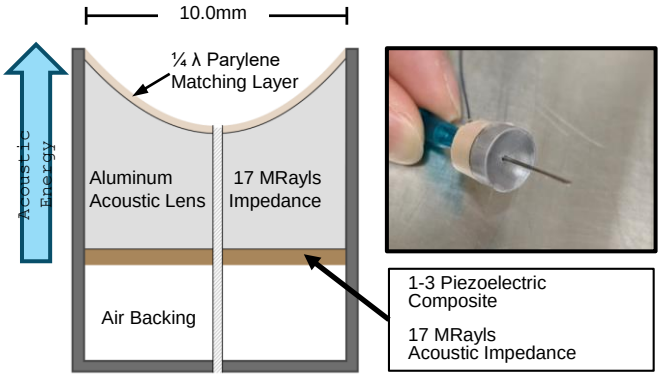

C

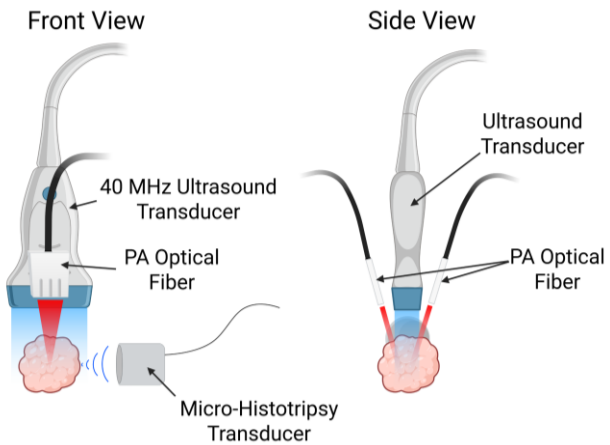

D

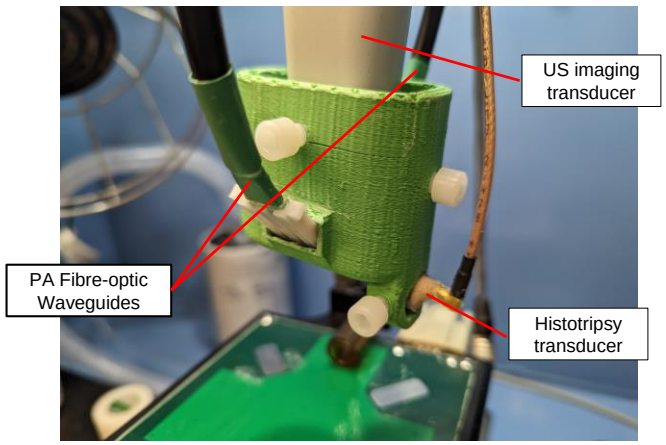

E

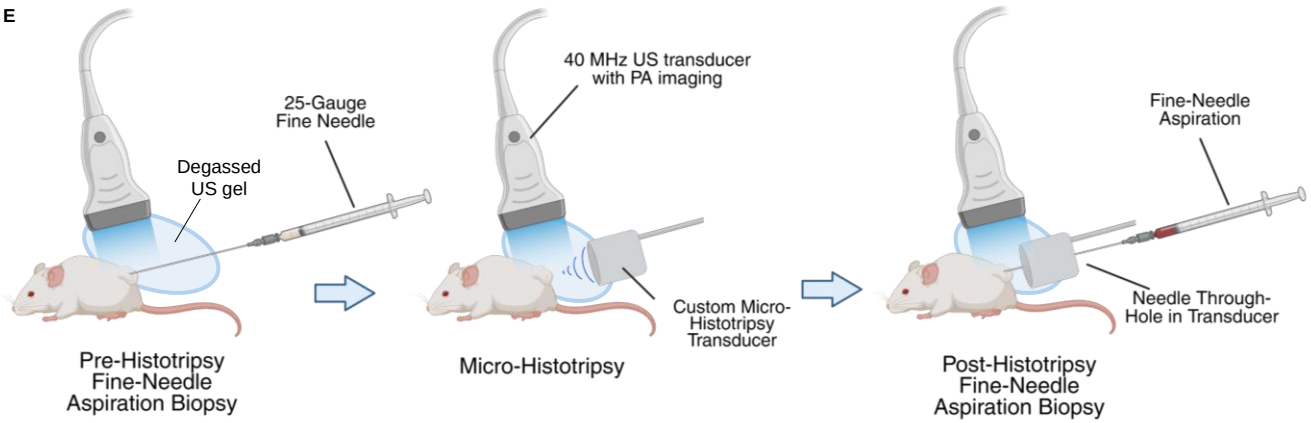

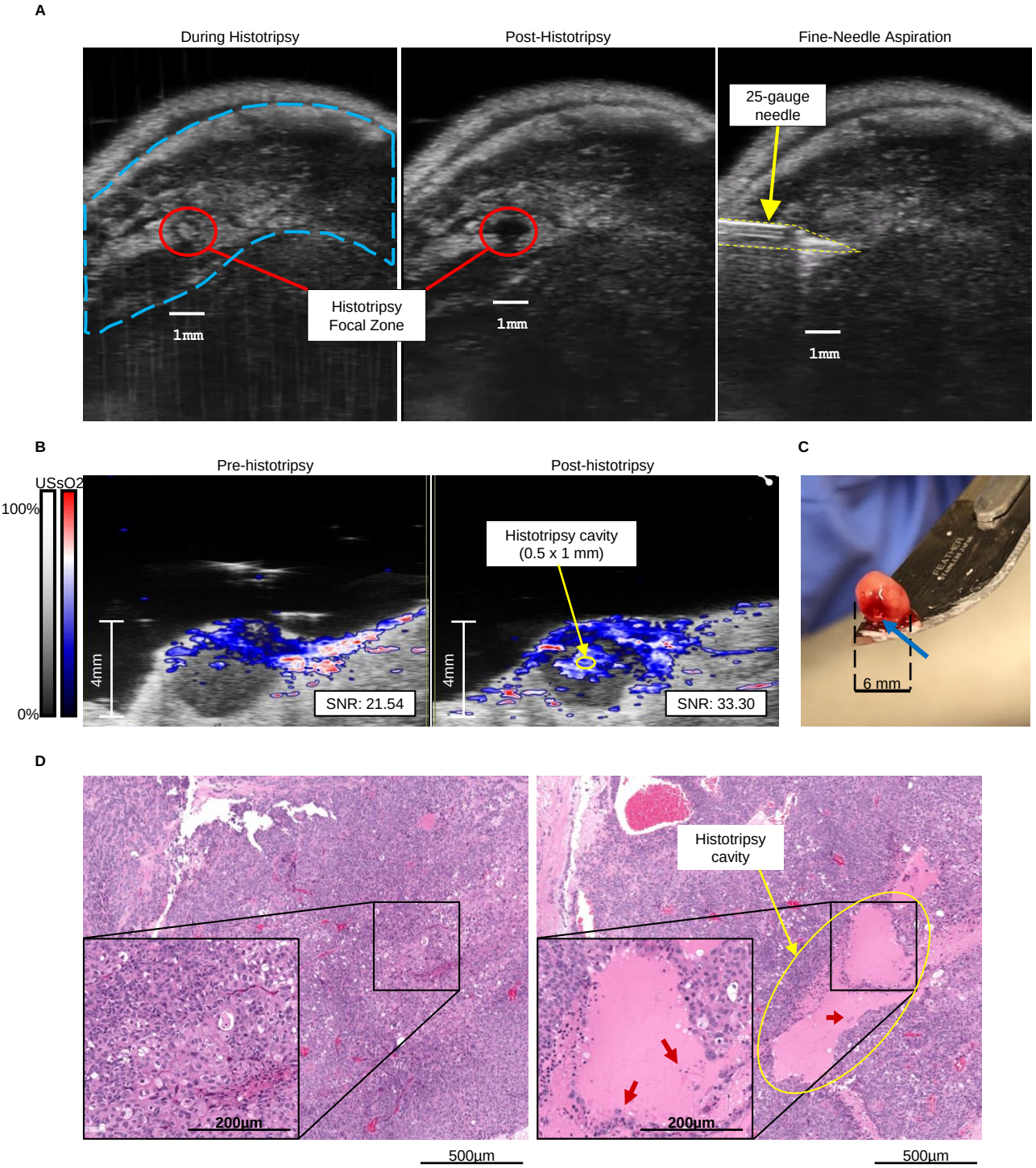
A
During Histotripsy
Post-Histotripsy
Fine-Needle Aspiration
Histotripsy
Focal Zone
1mm
1mm
25-gauge
needle
1mm
B
Pre-histotripsy
Post-histotripsy
USsO2
100%
0%
4mm
SNR: 21.54
Histotripsy cavity
(0.5 x 1 mm)
4mm
SNR: 33.30
C
6 mm
D
200µm
500µm
Histotripsy
cavity
200µm
500µm

A

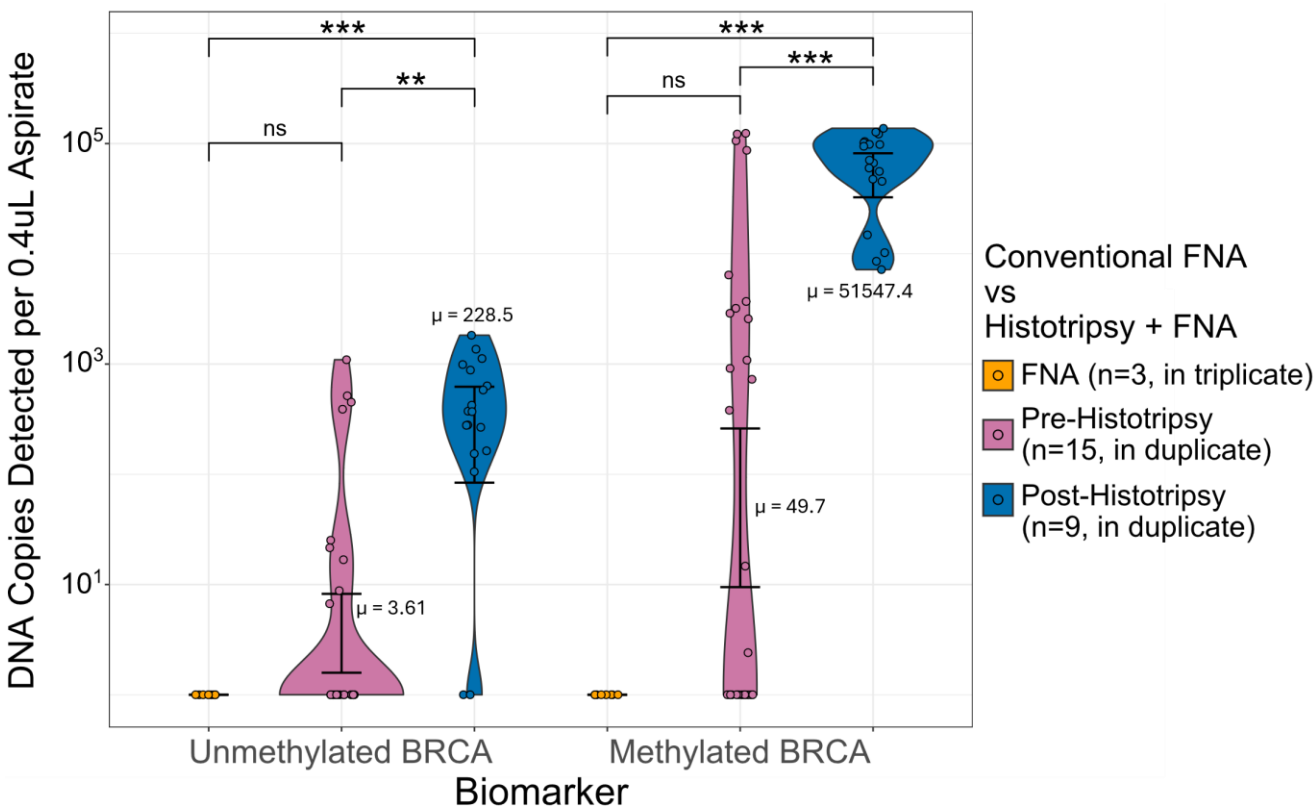
***
**
ns
***
***
ns
10^5
10^3
10^1
μ = 3.61
μ = 228.5
μ = 49.7
μ = 51547.4
DNA Copies Detected per 0.4uL Aspirate
Unmethylated BRCA
Methylated BRCA
Biomarker
Conventional FNA
vs
Histotripsy + FNA
FNA (n=3, in triplicate)
Pre-Histotripsy
(n=15, in duplicate)
Post-Histotripsy
(n=9, in duplicate)

B

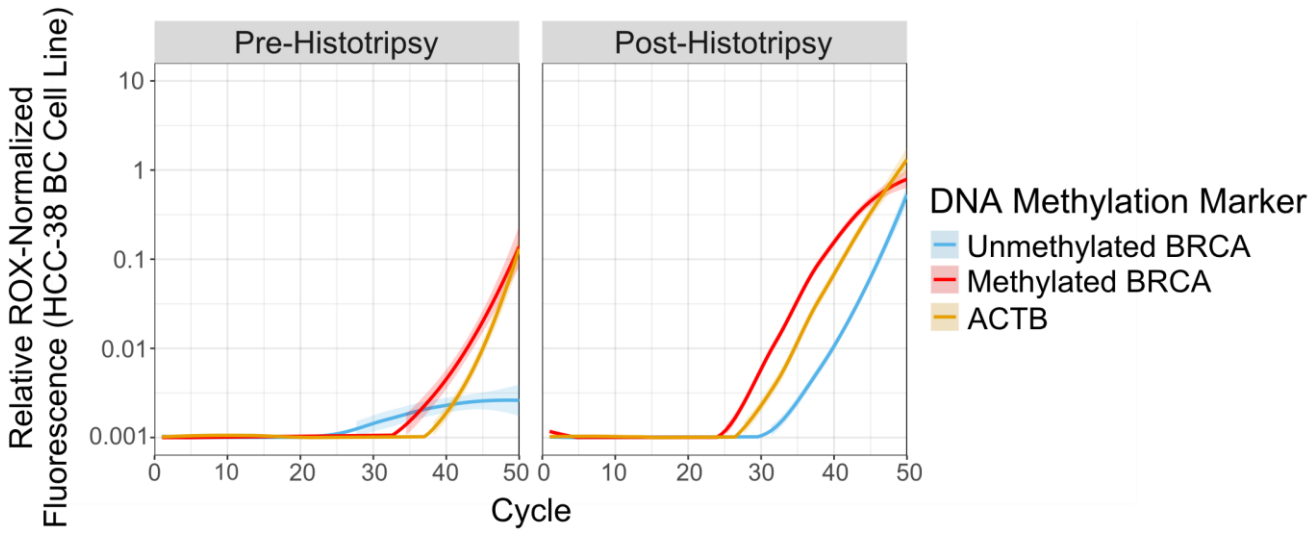
Pre-Histotripsy
Post-Histotripsy
10
1
0.1
0.01
0.001
0
10
20
30
40
50
Relative ROX-Normalized
Fluorescence (HCC-38 BC Cell Line)
Cycle
DNA Methylation Marker
Unmethylated BRCA
Methylated BRCA
ACTB

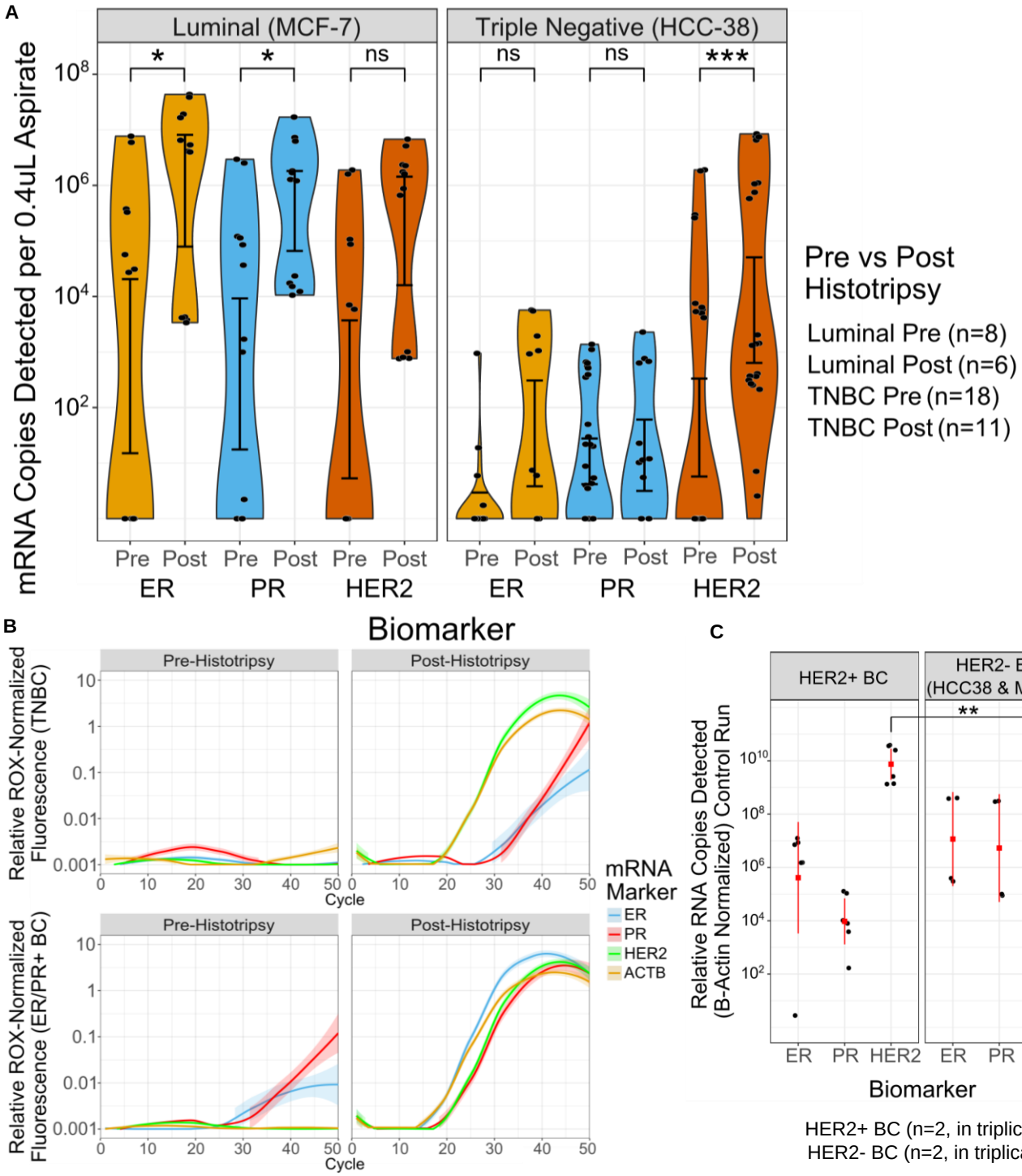
A
Luminal (MCF-7)
Triple Negative (HCC-38)
mRNA Copies Detected per 0.4uL Aspirate
10^8
10^6
10^4
10^2
*
*
ns
ns
ns
***
Pre Post Pre Post Pre Post
ER PR HER2
Pre vs Post Histotripsy
Luminal Pre (n=8)
Luminal Post (n=6)
TNBC Pre (n=18)
TNBC Post (n=11)
B
Biomarker
Pre-Histotripsy
Post-Histotripsy
Relative ROX-Normalized Fluorescence (TNBC)
Relative ROX-Normalized Fluorescence (ER/PR+ BC)
10
1
0.1
0.01
0.001
0 10 20 30 40 50
Cycle
mRNA Marker
ER
PR
HER2
ACTB
C
HER2+ BC
HER2- BC (HCC38 & MCF7)
**
Relative RNA Copies Detected (B-Actin Normalized) Control Run
10^{10}
10^8
10^6
10^4
10^2
ER PR HER2 ER PR HER2
Biomarker
HER2+ BC (n=2, in triplicate)
HER2- BC (n=2, in triplicate)

A

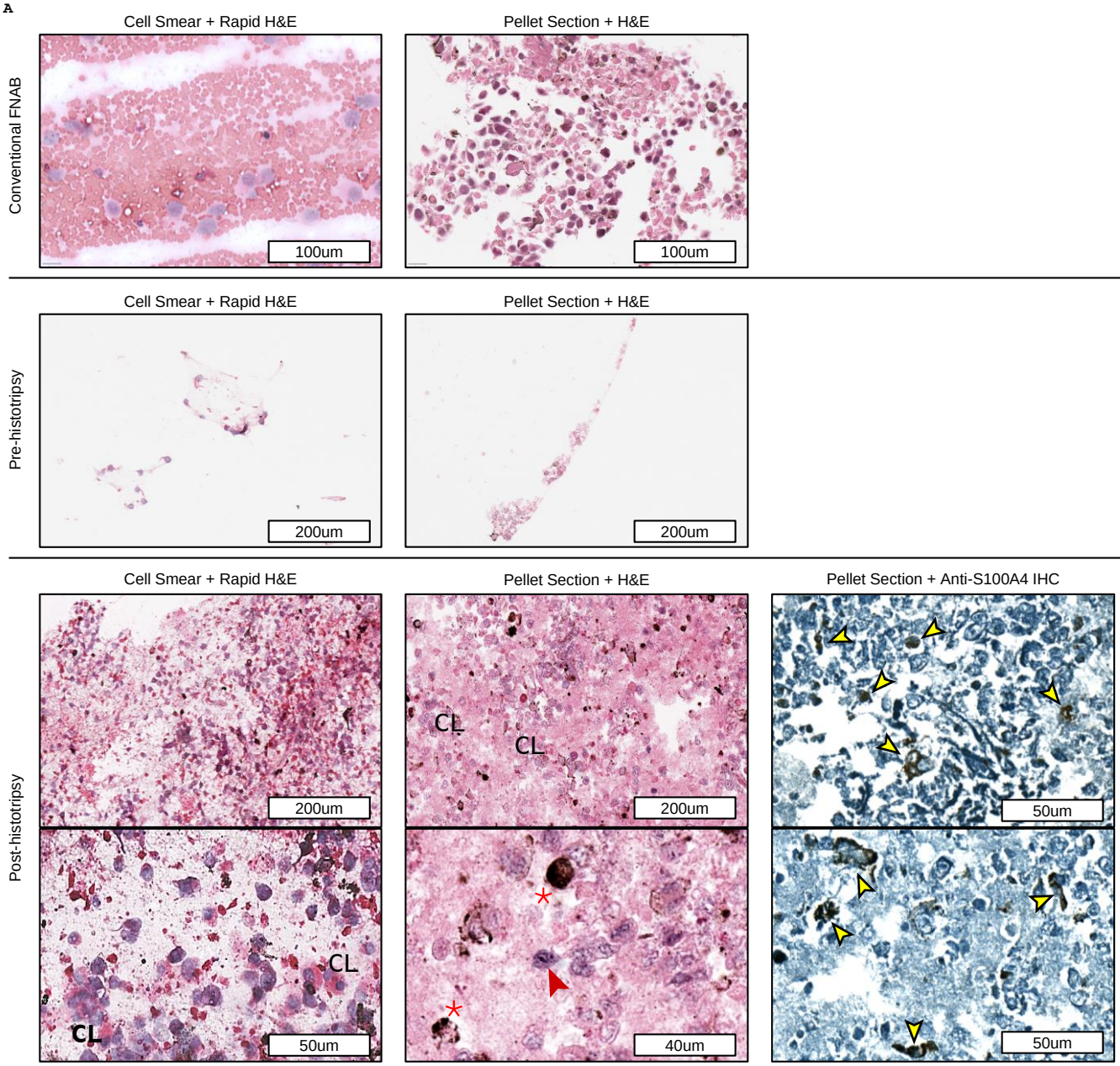

B

	FNA Smears	Histotripsy Smears	FNA Pellets	Histotripsy Pellets
Mean Cells per 40x FOV (95% CI)	30.76 ± 4.58	75.10 ± 8.15	52.21 ± 12.54	165.70 ± 59.34

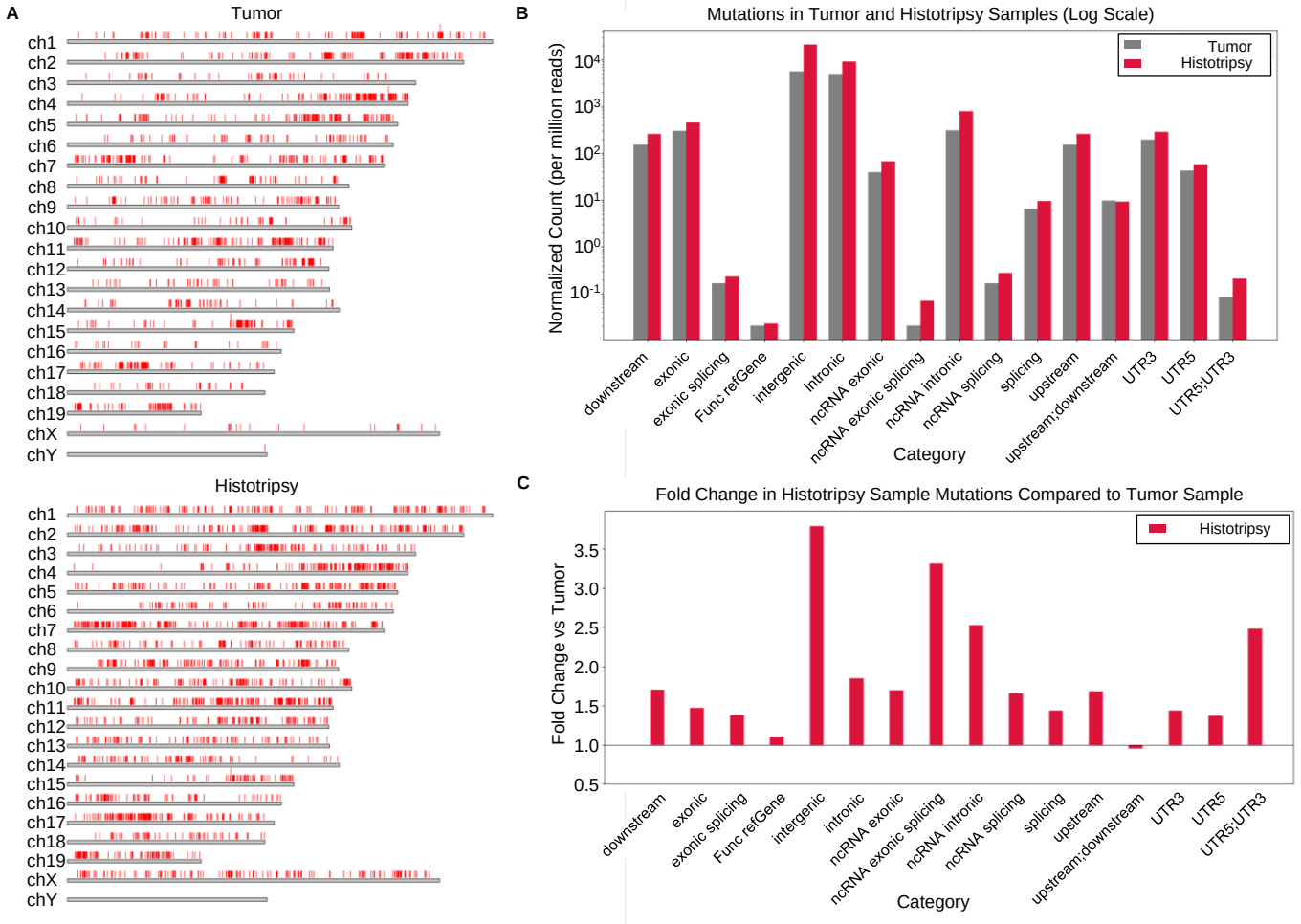
A
Tumor
ch1
ch2
ch3
ch4
ch5
ch6
ch7
ch8
ch9
ch10
ch11
ch12
ch13
ch14
ch15
ch16
ch17
ch18
ch19
chX
chY
Histotripsy
ch1
ch2
ch3
ch4
ch5
ch6
ch7
ch8
ch9
ch10
ch11
ch12
ch13
ch14
ch15
ch16
ch17
ch18
ch19
chX
chY
B
Mutations in Tumor and Histotripsy Samples (Log Scale)
Tumor
Histotripsy
Normalized Count (per million reads)
10^{4}
10^{3}
10^{2}
10^{1}
10^{0}
10^{-1}
downstream
exonic
exonic splicing
Func refGene
intergenic
intronic
ncRNA exonic
ncRNA exonic splicing
ncRNA intronic
ncRNA splicing
splicing
upstream
upstream;downstream
UTR3
UTR5
UTR5;UTR3
Category
C
Fold Change in Histotripsy Sample Mutations Compared to Tumor Sample
Histotripsy
Fold Change vs Tumor
3.5
3.0
2.5
2.0
1.5
1.0
0.5
downstream
exonic
exonic splicing
Func refGene
intergenic
intronic
ncRNA exonic
ncRNA exonic splicing
ncRNA intronic
ncRNA splicing
splicing
upstream
upstream;downstream
UTR3
UTR5
UTR5;UTR3
Category